Research Square

Preprints are preliminary reports that have not undergone peer review.
They should not be considered conclusive, used to inform clinical practice,
or referenced by the media as validated information.

Modeling Framework for Reinforced Concrete Buildings to Assess the Performance of Cast-in-Place Diaphragms with Openings

Pratik Patra

ppatra@uw.edu

University of Washington

Travis E. Thonstad

University of Washington

Dawn E. Lehman

University of Washington

Research Article

Keywords: Slab–frame interaction, Diaphragm load paths, Membrane-force distribution, Seismic demand, Nonlinear analysis

Posted Date: November 20th, 2026

DOI: https://doi.org/10.21203/rs.3.rs-11546051/v1

License: This work is licensed under a Creative Commons Attribution 4.0 International License.
Read Full License

Additional Declarations: No competing interests reported.

TITLE:

Modeling Framework for Reinforced Concrete Buildings to Assess the Performance of Cast-in-Place Diaphragms with Openings

AUTHOR BY LINE:

Pratik Patra[1], Travis E. Thonstad[2] and Dawn E. Lehman[3]

[1]Postdoctoral Associate, Department of Civil and Environmental Engineering, University of Washington, Seattle, WA, USA [Email: ppatra@uw.edu; iD - 0000-0001-8949-100X)]

[2]Assistant Professor, Department of Civil and Environmental Engineering, University of Washington, Seattle, WA, USA

[3]Professor, Department of Civil and Environmental Engineering, University of Washington, Seattle, WA, USA

ABSTRACT

Assessing cast-in-place reinforced concrete slabs, or diaphragms, with openings requires a nonlinear model that captures the dynamic demands developed by the building and their transfer through the slab. This paper presents a three-dimensional modeling framework, that retains the two-way interaction between diaphragms and vertical structural elements as cracking and inelastic deformation develop. Layered shells with nonlinear concrete and reinforcement models represent slabs and walls, fiber elements represent beams and columns, and discrete springs account for joint deformation and reinforcement slip, so diaphragm force paths develop without predefined chords, collectors, or struts. Component parameters are calibrated against five cyclic subassembly tests, and building response is validated against shake-table tests of a full-scale, five-story reinforced-concrete building with diaphragm openings, under motions spanning serviceability to maximum-considered-earthquake levels. Design-level peak drifts are predicted within 6%, and simulated crack fields reproduce the principal regions of observed slab damage near columns and openings, supporting interpretation of the unmeasured membrane forces. During stronger motions, tensile demand spreads over larger slab areas, while compression remains concentrated near openings and vertical elements. Force distributions differ between floor-force and drift peaks and between loading directions, indicating that a single peak-response configuration cannot describe the evolving load path. Biaxial tension, tension–compression, and biaxial compression coexist under unidirectional shaking, whereas the equivalent-beam idealization assumes pure shear. The framework supports future studies of other building archetypes, opening configurations, and diaphragm design idealizations.

KEYWORDS

Slab–frame interaction; Diaphragm load paths; Membrane-force distribution; Seismic demand; Nonlinear analysis

1 INTRODUCTION

Compared with the extensive research over the last 30 years devoted to the vertical elements of a building's lateral-force-resisting system (LFRS), such as shear walls or moment frames, the seismic response of the horizontal elements of a building's LFRS, the floor diaphragms, have received far more limited attention, particularly in the case of cast-in-place (CIP) reinforced concrete diaphragms. A typical diaphragm must collect the inertia forces generated by the floor mass and transfer them to the vertical elements of the LFRS. At the same time, the diaphragm must also tie together frames, walls, columns, and gravity-system components and enforce compatible movement among vertical elements with different stiffnesses and inelastic response characteristics. A diaphragm also universally contains openings, which occur over a wide range of scales. Large openings accommodate stairs, elevators, and atria; intermediate openings serve mechanical and ventilation shafts; and smaller penetrations accommodate piping, electrical services, and other utilities.

Diaphragm forces, therefore, arise not only from floor inertia but also from compatibility and transfer actions generated through interaction with the vertical system (Bull 2004; Moehle et al. 2016; Godínez and Restrepo 2023). In a CIP building, these functions are performed by the same monolithic slab that carries gravity loading. The resulting seismic force path is complex, with distributed forces through the slab, and concentrated forces around wall–slab and slab–frame connections. In design, this force path is commonly represented by an equivalent-beam idealization, in which the diaphragm spans between vertical elements as a deep beam: chords along the slab edges resist the in-plane moment, and the slab between them carries a uniform shear flow and is therefore in a state of pure shear (Moehle et al. 2016). Simultaneously, openings in the floor slab interrupt this force path, raising local force demands and reducing connection capacity if the openings are located near columns or walls. Understanding how forces flow around these openings can therefore guide their placement and detailing to limit slab damage during seismic loading.

While well-designed CIP diaphragms have generally performed adequately in past earthquakes, loss of horizontal continuity in the diaphragm, potentially intensified by the presence of openings, can compromise the ability of otherwise intact vertical elements to participate in resisting lateral forces and may increase the risk of building collapse. Several notable cases from post-earthquake reconnaissance exemplify this risk, including the tragic collapse of the Canterbury Television building the 2011 Christchurch earthquake, which was partially attributed to deficiencies in the connections between the floor diaphragms and the north wall complex (Canterbury Earthquakes Royal Commission 2012; Scarry 2014) and the partial collapse of the MCG Tower following the 2023 Kahramanmaraş earthquake sequence, which was attributed to inadequate transfer of seismic forces through the slabs to the elevator-core walls (Vuran et al. 2025). In addition to these well-documented failures, other cases of diaphragm-related damage may have gone undocumented in previous

reconnaissance studies. Loss of horizontal force transfer can initiate cascading damage in the diaphragm, its connections, and the LFRS. Once partial or total collapse occurs, the original diaphragm damage may be obscured, making the initiating mechanism difficult to reconstruct from forensic evidence. Consequently, some diaphragm-initiated failures may be recorded only as global structural collapse.

One of the key challenges with diaphragm-related research is the difficulty and expense of studying them under realistic boundary conditions and loads. Experimentally, monolithic CIP diaphragms cannot be easily subdivided into smaller test assemblies, suitable for typical laboratories, and large shaking table tests are time-consuming and require specialized laboratories that are expensive to operate, thus limiting the number of parameters that can be investigated experimentally. Numerically, nonlinear finite-element simulation enables many more parameters to be considered (fib 2008; ACI Committee 374 2016), however these models must be sufficiently complex to simultaneously satisfy two conditions:

- The dynamic force arriving at the diaphragm must be reproduced accurately, including the effects of higher modes, mass distribution, and progressive inelasticity of the vertical system. Parametric studies have shown that both diaphragm and LFRS stiffness and inelasticity affect building response and force demands (Al Harash 2011; Fischer and Schafer 2023a, b; Correal et al. 2020).
- The diaphragm representation must resolve how that force travels through the cracked slab, is redirected around openings, and enters the LFRS. Reduced-order approaches such as the nonlinear stringer-panel model have provided an efficient means of representing cracking in dynamic building analysis and have shown that diaphragm forces can redistribute substantially after cracking (Godínez and Restrepo 2023). However, the internal path in such models remains associated with a predefined network of stringers and panels.

Finite-element models that satisfy both conditions are computationally expensive, since they must capture the nonlinear response of every structural element of the building in high-fidelity. Satisfying only the first condition yields a credible global floor force but not the local design demands. Satisfying only the second may provide a detailed slab stress field under an inaccurate or artificially prescribed input. As illustrated in Fig. 1, this interaction is two-way because inelasticity can develop in both the vertical system and the diaphragm. The response of the vertical system imposes inertia and compatibility demands on the diaphragm, and these demands change in magnitude and distribution as the vertical elements crack and yield (Rodriguez et al. 2002; Fischer and Schafer 2023b). In turn, cracking and reinforcement yielding in the diaphragm reduce its in-plane stiffness and redistribute forces among the vertical elements, which modifies their response (Kunnath et al. 1991; Panahshahi et al. 1991; Fleischman and Farrow 2001). Most prior studies have represented inelasticity in the vertical system while treating the diaphragm as rigid or elastic, capturing only one side of this interaction

(Barron and Hueste 2004; Ruggieri et al. 2020; Fischer and Schafer 2023a; Pecce et al. 2017; Wei et al. 2023). A model must therefore retain the nonlinear response of both systems as loading progresses to relate global floor forces to local slab demands.

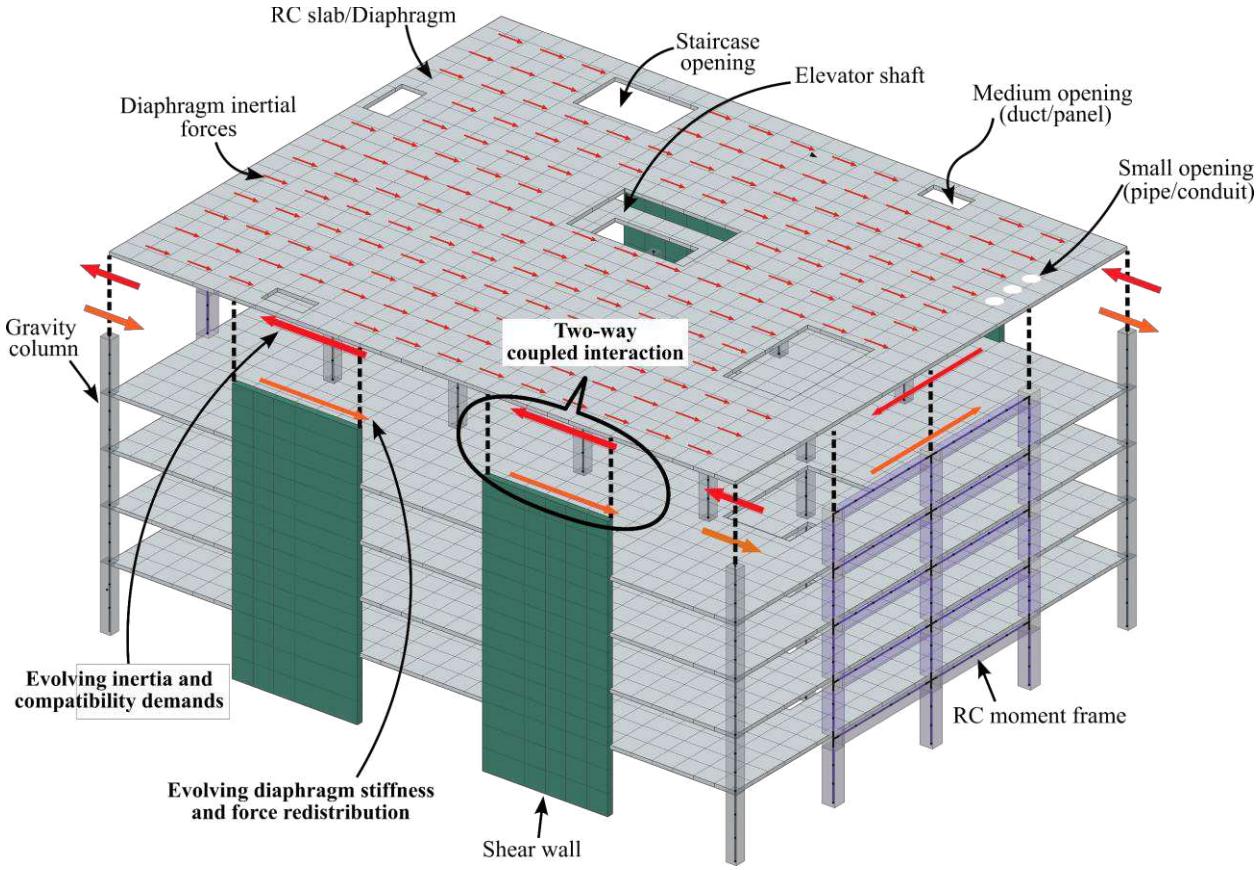


Fig. 1 Schematic of the two-way interaction between the diaphragm and the vertical structural elements in the nonlinear building model

Despite the inherent challenges in studying floor diaphragms, important advances have still been made, although this progress has been concentrated in selected construction systems. Rodriguez et al. (2002) demonstrated that higher-mode floor accelerations are unaffected by yielding of the lateral force resisting system, providing the analytical foundation for the first-mode reduced approach later incorporated into code-based design procedures (ASCE 2022). The Diaphragm Seismic Design Methodology program subsequently combined component tests, analytical studies, hybrid simulation, and shake-table testing to establish a performance-based design framework for precast concrete diaphragms (Fleischman et al. 2005a, b, Fleischman et al 2013; Schoettler et al. 2009; Zhang and Fleischman 2016; Zhang et al. 2019). For steel-deck and composite diaphragms, Eatherton et al. (2020) evaluated diaphragm ductility and overstrength using a large database of cantilever tests, while later system-level analyses examined the consequences of diaphragm inelasticity for steel buildings (Wei et al. 2023). While useful for the understanding of diaphragm response, these

developments do not transfer directly to monolithic CIP construction. Precast diaphragm response is governed largely by discrete joints and mechanical connectors, while steel-deck response is strongly influenced by deck geometry, orthotropy, and fastener deformation. In contrast, CIP diaphragms are monolithic elements in which the inelastic force path develops through distributed concrete cracking, tension stiffening, reinforcement yielding, aggregate interlock, and localized crushing. The regions of reduced stiffness are therefore created by the response rather than prescribed by construction joints or fastener lines.

Although precast and steel-deck systems have benefited from coordinated analytical and experimental research programs, no comparable program has established the global demand, deformation capacity, or system-level failure mechanisms of CIP diaphragms. Available analytical studies show why opening location and the continuity of the remaining slab matter alongside opening area. Khajehdehi and Panahshahi (2016) showed that openings alter the in-plane failure mechanism of RC slabs, introduce additional yielding at opening corners, and reduce in-plane capacity. Al Harash (2011) showed that neglecting inelastic diaphragm deformation can significantly underestimate interior-frame demands, particularly when openings are located within the middle two-thirds of the floor plan. These findings are particularly relevant when elevator, mechanical, or service openings occur close to walls and frame lines. In that configuration, the geometric discontinuity lies within the same region in which the diaphragm must collect and transfer large floor forces. Full-building nonlinear models with continuum slab representations are uncommon (Nebrijo et al. 2026; Zapata et al. 2026), with previous simulation of experimental shake-table specimens (Ebrahimian et al. 2018; Janevski et al. 2023) focusing primarily on global response, member deformation, and selected slab cracking rather than on the evolving diaphragm membrane forces.

This paper presents and verifies a modeling approach for CIP diaphragms with openings, capable of both accurately reproducing the dynamic forces arriving at the diaphragm level and resolving the load path through the slab with high fidelity. The proposed reduced-order modeling approach provides a deliberate intermediate level of resolution, preserving dynamic interactions within the building's structural systems while resolving the distributed slab membrane resultants needed to interrogate diaphragm force paths. Components of the modeling strategy were first calibrated against the results from cyclic beam-column and wall subassembly tests and then validated using the results from shake table tests of a multistory reinforced concrete building model, which contained slab openings. The experimentally validated framework provided a direct link between global building response, distributed diaphragm mechanics, and the localized regions in which damage was observed. The modeling approach is therefore useful for investigating both the risk of diaphragm damage during earthquakes, with potential impacts on resilience and functional-recovery objectives, and the

effectiveness of conventional diaphragm idealizations used in design and where opening-induced redistribution and nonlinear interaction with the vertical system create demands not apparent from these elastic methods.

2 COMPUTATIONAL MODELING APPROACH

The modeling framework resolves the seismic response of a reinforced concrete building at two interacting scales: the dynamic demand developed by the complete building and the distributed membrane-force field that transfers this demand through each diaphragm. The term framework here denotes a set of modeling requirements such as: (1) the dynamic force arriving at each floor be reproduced, including higher-mode effects, mass distribution, and the progressive inelasticity of the vertical system, and (2) the diaphragm be represented as a continuous nonlinear medium, so that the force path through the cracked slab, around openings, and into the LFRS develops from the analysis rather than being prescribed.

In this study, the framework was implemented in LS-DYNA, although any platform whose element formulations and constitutive models reproduce these mechanisms could be used. Slabs and walls were modeled with layered shell elements using nonlinear concrete and reinforcement material models, frame members with fiber-discretized beam–column elements, and localized joint-panel and reinforcement-slip deformations with discrete springs. The equations of motion were solved by explicit time integration.

The model was reduced through sectional discretization rather than through an assumed diaphragm load path: member cross sections were represented by shell layers, while the diaphragm remained a continuous two-dimensional finite-element mesh. This provided a practical intermediate resolution between rigid or elastic diaphragm idealizations (ASCE 2022; CEN 2004b), which cannot recover nonlinear membrane-force redistribution, and three-dimensional solid models, which are generally too computationally demanding for complete-building nonlinear response-history analysis. For reference, in the current study the LS-DYNA simulations were performed using SKX compute nodes on the Stampede3 supercomputer at the Texas Advanced Computing Center (TACC) at the University of Texas at Austin. A representative ground-motion analysis for the verification model required approximately 60,000 allocated CPU core-hours, with computational cost varying among input records.

2.1 Element Formulations and Section Discretization

Floor slabs and walls were modeled using four-node Belytschko–Lin–Tsay shell elements (ELFORM 2; Belytschko et al. 1984). The element uses a co-rotational, first-order shear-deformable formulation with reduced integration in the element plane. As shown in Fig. 2a, integration points were assigned through the shell thickness using a layered composite section. Concrete and orthogonal reinforcement layers were placed at their corresponding section elevations. The shell kinematics imposes compatible strains on the concrete and

reinforcement layers. Concrete carries normal and shear stresses before cracking and retains compression and crack-plane shear transfer after cracking. The reinforcement layers provide axial resistance along the prescribed bar directions and dowel resistance across open cracks. Each layer evaluates its own constitutive response under the imposed strains, permitting concrete cracking, reinforcement yielding, neutral-axis migration, and membrane–flexural interaction to develop through sectional integration. The stresses developed by the individual layers are integrated through the thickness. The reinforcement fractions and material directions can be specified independently in the two local slab directions, allowing different top- and bottom-mat reinforcement ratios to be represented. The concrete and reinforcement layers remain strain compatible; localized bond slip is introduced separately through the connection model rather than within the distributed shell section.

Columns and frame beams were represented using Hughes–Liu beam elements (ELFORM 1; Hughes and Liu 1981) with cross sections discretized into concrete and reinforcement fibers, as illustrated in Fig. 2b. Confined core concrete, unconfined cover concrete, and longitudinal reinforcing bars can therefore be assigned separate constitutive responses at their physical locations. Axial–flexural interaction, reinforcement yielding, neutral-axis migration, and cyclic section response emerge from fiber integration.

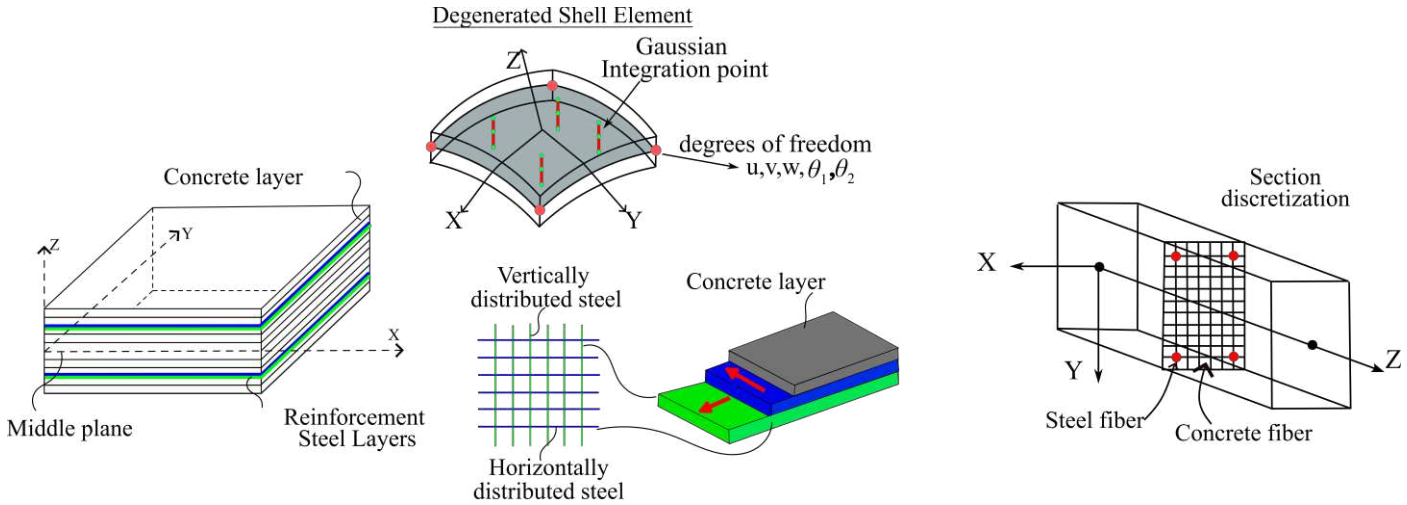


Fig. 2 Section discretization used in the numerical model: (a) layered-shell representation of slabs and walls with concrete and orthogonal smeared-reinforcement layers; and (b) fiber-discretized Hughes–Liu beam section for frame members

2.2 Concrete Constitutive Model

Concrete in the shell layers and beam fibers was represented using *MAT_CONCRETE_EC2 (MAT_172). The formulation was developed for reinforced-concrete shell and beam analyses and combines

nonlinear compression with a nonrotating, multidirectional smeared-crack representation of tension. Shell integration points were evaluated under plane-stress conditions, whereas concrete fibers in the beam sections carry uniaxial stress. The material was initially isotropic; however, once cracking occurs, its response becomes direction dependent on the local crack coordinate system. The tensile response was regularized by a tensile fracture energy, whereas the descending compression branch is strain based and highly localized crushing may therefore remain mesh sensitive. This concrete material model was selected to capture distributed membrane–flexural cracking, cyclic stiffness degradation, and force redistribution, but was not capable of simulating a three-dimensional punching-shear mechanism. Localized confinement, inclined critical shear cracking, and punching-cone geometry at slab–column connections lie outside the plane-stress kinematics of the layered shell. Accordingly, the numerical results are interpreted through membrane and connection force resultants and distributed crack patterns rather than predictions of a punching failure surface.

Fig. 3(a) shows, schematically, the uniaxial stress-strain response for compression and tension for unconfined and confined concrete used in the modeling approach. For unconfined concrete, the ascending compression envelope was modeled using the relationship proposed by CEN (2004a) & LST 2023),

$$\sigma = f_c \left[\frac{3(\varepsilon/\varepsilon_{c1}^{u})}{2+(\varepsilon/\varepsilon_{c1}^{u})^3}\right] \qquad 0 \le \varepsilon_c \le \varepsilon_{c1}^{u} \qquad (1)$$

where f_c is the unconfined compressive strength and ε_{c1}^{u} is the corresponding peak strain. Beyond the peak ε_{csp}^{u}, the unconfined envelope decreased to zero at the specified ultimate compressive strain. Confined concrete was represented using the Mander relationship (Mander et al. 1988),

$$\sigma = f_{cc} \frac{r(\varepsilon/\varepsilon_{c1}^{c})}{r-1+(\varepsilon/\varepsilon_{c1}^{c})^r} \qquad r = \frac{E_c}{E_c - f_{cc}/\varepsilon_{c1}^{c}} \qquad (2)$$

where f_{cc} and ε_{c1}^{c} are the confined compressive strength and its corresponding strain, and E_c is the initial modulus of elasticity of the concrete. In Fig. 3(a), ε_{csp} denotes the strain at which the unconfined cover concrete spalls.

Tensile cracking initiated when the maximum in-plane principal tensile stress reached f_t. The first crack direction was stored when the crack formed and remained fixed during subsequent loading. Additional crack families could develop at prescribed orientations when the tensile criterion was reached in a new direction. This multidirectional fixed-crack capability was important under cyclic diaphragm response because the principal membrane-force direction can change as loading reverses and force redistributes around openings.

Cracks may close under compression and reopen during subsequent tensile excursions. In Fig 3(b), ε_t is the strain at the onset of tensile cracking, and ε_{t1} is the strain at which the tensile stress decreases to zero.

Following crack initiation, the tensile stress decreased according to the bilinear tension-stiffening relation shown in Fig. 3b. The retained tensile resistance represents the contribution of concrete between cracks in a reinforced-concrete continuum. Tensile softening was expressed in terms of the crack-opening displacement

$$w = L_{\mathrm{char_c}}\varepsilon_{\mathrm{c}} \tag{3}$$

$$w_u = L_{\mathrm{char_c}}\varepsilon_{tu} \tag{4}$$

where ε_{c} is the crack-opening strain, ε_{tu} is the strain at complete tensile softening, and $L_{\mathrm{char_c}}$ is the characteristic crack-band length. Consequently, the effective energy, G_h, dissipated per unit crack area was given by the integral of the tensile stress-crack opening displacement curve from 0 to w_u, with the characteristic-length transformation keeping the crack-opening displacement, rather than the terminal crack-opening strain, approximately independent of element size. It therefore controlled tensile localization in the sense of the crack-band approach of Bažant and Oh (1983). In MAT_172, G_h is implied by f_t, the softening parameters, and $L_{\mathrm{char_c}}$; it is not entered as an independent fracture-energy parameter. The same characteristic length is also used as the crack spacing in the aggregate-interlock formulation.

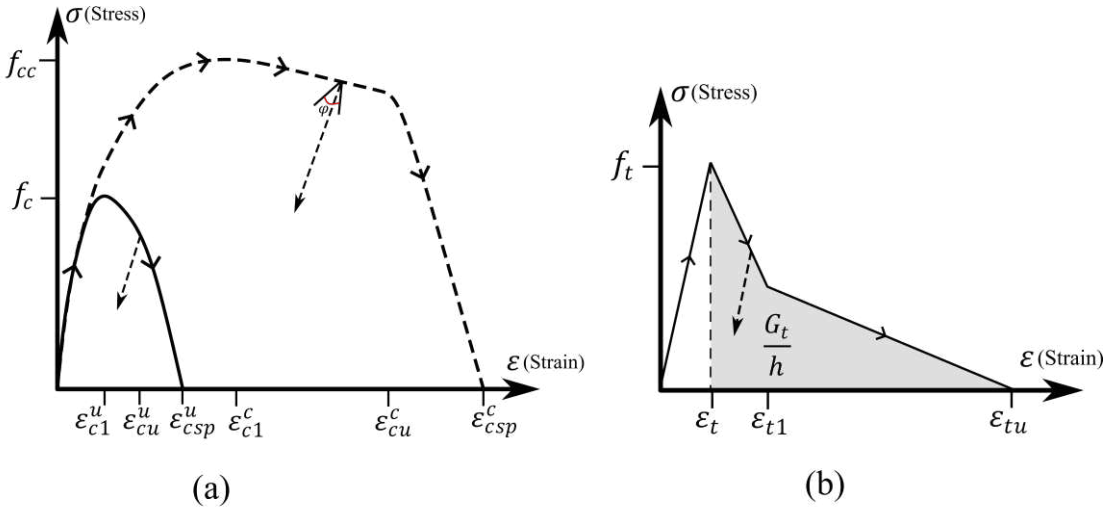


Fig. 3 Constitutive responses used in the numerical model: (a) unconfined and confined concrete compression envelopes; (b) characteristic-length-adjusted post-cracking tension-stiffening relation

After cracking, the model represents several mechanisms that govern the evolving concrete response. Aggregate interlock transfers shear across open cracks as a function of crack width, aggregate size, tensile strength, and compression normal to the crack, while compression softening reduces the concrete resistance parallel to a crack as transverse tensile strain develops. Cyclic unloading and reloading further account for stiffness degradation, permanent compressive strain, crack closure, and recovery of compressive resistance after closure. Together, these features allow the diaphragm stiffness and internal membrane-force field to evolve as cracking accumulates. More information about the features of the model can be found in LS-DYNA Keyword User's Manual, Volume II (LST 2023).

2.3 Reinforcement Constitutive Model

Reinforcement in the layered shells and beam fibers was represented using *MAT_HYSTERETIC_REINFORCEMENT (MAT_203). The model treated the reinforcement as independent uniaxial components acting along the assigned local bar directions. Reinforcement area was introduced through the orthogonal steel fractions in the shell layers or through the individual bar-fiber areas in the beam sections. User-defined tensile and compressive stress–strain curves permit yielding, strain hardening, and non-bilinear monotonic behavior to be represented without imposing a common idealized backbone on all reinforcement types.

Under load reversal, the transition between the tensile and compressive envelopes followed a smooth curve controlled by a power-law curvature parameter. Bar buckling was represented by degradation of the compressive envelope following tensile yielding, based on either an effective bar slenderness or a prescribed buckling strain and post-buckling slope. This approach represents the average stress–strain response of a bar segment between effective lateral restraints rather than the local curvature of an individual buckled bar (Dhakal and Maekawa 2002).

Cumulative cyclic deterioration is governed by the accumulated absolute plastic strain, κ_p, where increments developed in both tension and compression contribute positively (LST 2023). Strength and stiffness remained unchanged until κ_p reached the specified damage-initiation threshold, then strength and stiffness decreased toward a prescribed residual fraction at the complete-damage threshold. This provided phenomenological representation of progressive cyclic degradation.

Dowel action represented the local bending of reinforcing bars against the surrounding concrete, providing shear resistance across cracks in addition to aggregate interlock. The dowel response was idealized as elastic–perfectly plastic. The initial stiffness was based on the beam-on-elastic-foundation approach described by El-Ariss (2007), incorporating the concrete bearing stiffness relationship proposed by Soroushian

et al. (1987). The limiting dowel shear stress was obtained by dividing the limiting dowel force attributed to Dulacska (1972) by the bar cross-sectional area:

$$\tau_{yb} = 1.62\sqrt{f_c f_y} \quad (5)$$

For the simplified formulation with negligible crack width and a unit bar-spacing coefficient, the initial equivalent shear modulus was expressed as:

$$G = 8.02 {E_s}^{0.25} {f_c}^{0.375} L_{\text{char}} {d_b}^{-0.75} \quad (6)$$

where f_c is the compressive strength of the surrounding concrete, f_y is the reinforcement yield strength, E_s is the steel elastic modulus, d_b is the bar diameter, and L_{char} is the characteristic deformation length used to convert crack slip to shear strain. The stiffness expression uses stresses and elastic moduli in MPa and lengths in mm. Dowel action was incorporated as a constitutive shear-transfer mechanism within the composite section. Together with aggregate interlock, it provided postcracking shear resistance and contributed to force redistribution as cracking and reinforcement nonlinearity developed.

2.4 Beam–Column Joint Modeling

Adequately capturing beam-column joint flexibility is crucial for reproducing the dynamic forces arriving at the floor, including the progressive inelasticity of the vertical system. The assumption of rigid joints and fully bonded reinforcement both lead to unrealistic frame stiffness, impacting the magnitude and distribution of dynamic forces and may lead to premature bar fracture due to stress concentrations at the beam-column connections. The adopted modeling approach incorporated both bond slip and joint-panel shear flexibility mechanisms, in addition to cyclic beam flexural hinging, which was handled automatically by the fiber-based beam elements. Member shear failure was not included in this representation; therefore, the validation is limited to frames where flexure is the predominant deformation mode.

Beam–column joint flexibility in the moment-resisting frames was represented using a simplified two-dimensional macro-model based on the scissors idealization of Alath and Kunnath (1995) and the two-spring formulation of Grande et al. (2021a, b), as illustrated in Fig. 4. This model was selected over more sophisticated methods (e.g., Lowes 2003) for simplicity in connection with diaphragm elements, recognizing joint damage and distress were not the focus of the present modeling effort. The representative connection (geometrically relevant for the shake table test specimen used for validation) comprised a column, continuous above and below the joint, and one beam framing into the column joint. The effects of the slab, transverse framing, out-of-plane confinement, and beam–column eccentricity were excluded from this local idealization. Beam and column axial–flexural response, including concrete cracking, reinforcement yielding, and plastic-hinge development,

was represented directly by the adjoining fiber-discretized elements. No separate flexural-hinge spring was introduced. The joint macro-model, therefore, only adds the two deformation mechanisms not represented explicitly by the member fiber sections: joint-panel shear deformation and the fixed-end rotation produced by beam-reinforcement slip and strain penetration. This arrangement is consistent with the exterior-joint scissors model, in which two rotational springs act in series while the surrounding frame members retain their own flexural response. Each spring was modeled as a zero-length discrete-beam element governed by *MAT_GENERAL_NONLINEAR_6DOF_DISCRETE_BEAM (MAT_119), with nonlinear behavior assigned to the in-plane rotational degree of freedom. The discrete-beam formulation permits zero initial length and provides independent force–deformation relations for as many as six local degrees of freedom, although only one was necessary here (LST 2023). For both rotational springs, unloading option was specified as IUNLD=3, producing quadratic unloading from peak displacement value to a permanent offset. The complete loading, unloading, and reloading curves were calibrated against the response of subassembly test specimens to reproduce the measured pinching, residual deformation, and cyclic stiffness and strength degradation of the specimens. Thus, the cyclic response of moment frame connections were a product of both the calibrated spring laws and the selected unloading formulation, rather than from the unloading option alone. The calibrated two-spring formulation was subsequently retained in the building model to ensure that these deformation mechanisms were represented consistently from the component to the system level.

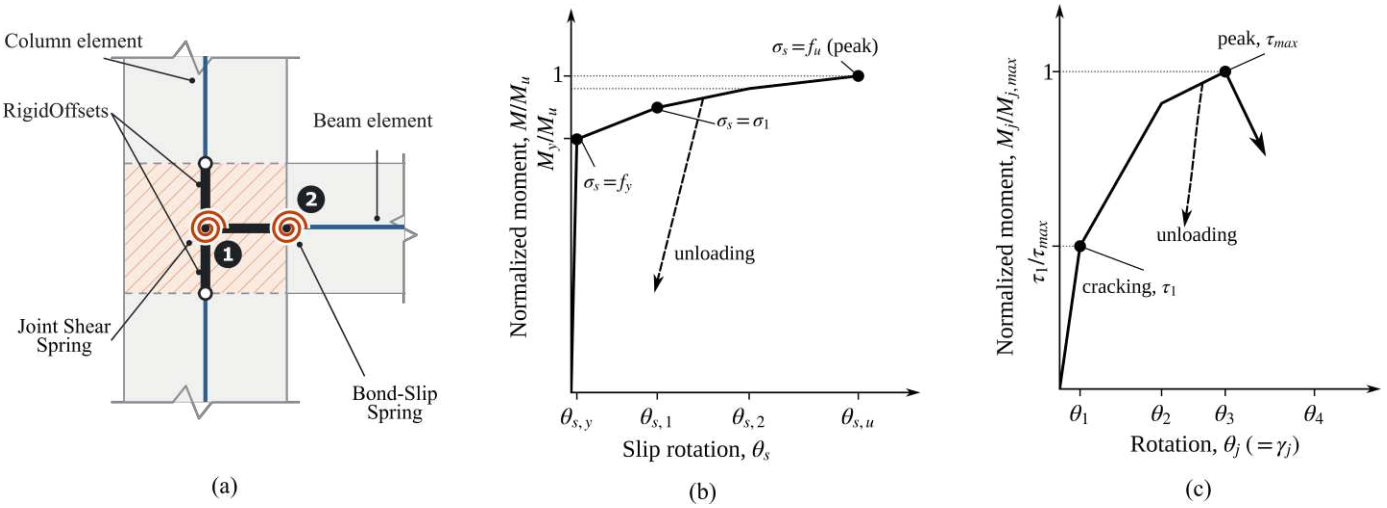


Fig. 4 (a) Beam–column joint idealization; (b) normalized bond-slip spring backbone; (c) normalized joint shear spring backbone

Fig. 4(b) shows, schematically, the normalized bond-slip backbone adopted in the modeling approach. The fixed-end rotation concentrated at the beam–joint interface due to the penetration of bar strains into the joint anchorage was modeled using the idealization described by Lowes et al. (2004) in the discretized form presented by Bao et al. (2014). A stepped uniform bond-stress distribution was assumed along the embedded

bar. An average bond stress $\tau_e$was assigned for strains smaller than yield strain, while a reduced average bond stress $\tau_y$was assigned over the yielded anchorage length. For a discretized monotonic reinforcement stress–strain relation consisting of successive points $(\varepsilon_s, \sigma_s)_n$, the loaded-end slip was calculated as

$$s_{n+1} = \begin{cases} (\varepsilon_s)_{n+1}(\sigma_s)_{n+1}\frac{d_b}{8\tau_e} & (\sigma_s)_{n+1} \le f_y, \\ s_n + [(\varepsilon_s)_{n+1} + (\varepsilon_s)_n][(\sigma_s)_{n+1} - (\sigma_s)_n]\frac{d_b}{8\tau_y} & (\sigma_s)_{n+1} > f_y, \end{cases} \quad (7)$$

where σ_s is the bar stress, τ_b is the average bond stress, and d_b is the bar diameter and $s_1 = 0$. Unlike closed-form models based on an idealized bilinear reinforcement response, Eq. (7) accepts an arbitrary monotonically increasing stress–strain curve. This capability is important for the incorporation of high-strength reinforcement, which does not exhibit a distinct yield plateau.

At reinforcement stress level, the beam-interface moment was obtained from equilibrium of the corresponding fiber section. The associated fixed-end rotation, θ_s, was calculated from the loaded-end slip using the rigid-body kinematics, $\theta_s = \mathrm{s}/(d - d')$, where $d - d'$ is the distance between the tension and compression reinforcement resultants. Separate positive and negative backbone branches were generated where the reinforcement arrangement or measured material response differed between the two loading directions. Because beam flexural cracking and distributed curvature were already represented by the fiber-discretized beam elements, the initial branch of the strain-penetration spring was made effectively rigid to avoid counting pre-yield flexural flexibility twice, consistent with the modification adopted by Grande et al. (2021a). The spring became active as reinforcement yielding develops and inelastic strain penetrates into the anchorage. No anchorage-strength limit or pullout failure branch was introduced, recognizing that these failure mechanisms were not observed in the calibration and validation test specimens and were not the focus of the current modeling effort.

Fig. 4c shows, schematically, the normalized joint shear spring backbone adopted in the modeling approach. The joint-panel response was defined by a multilinear shear stress–strain backbone comprising four characteristic points, representing diagonal cracking (τ_1, γ_1), pre-peak response (τ_2, γ_2), maximum resistance (τ_3, γ_3), and residual resistance (τ_4, γ_4). For the adopted two-dimensional idealization, the effective joint width, b_j, was taken equal to the column width. The joint-panel area, A_j, was calculated as the product of the effective joint width and the column depth parallel to the frame, h_c. The average column axial stress was calculated as the quotient of the column axial force, *N* (taken as positive in compression), and the joint-panel area. The joint cracking stress was calculated using the expression proposed by Uzumeri (1977),

$$\tau_1 = 0.29\sqrt{f_c'}\sqrt{1 + 0.29\sigma_j} \quad (8)$$

where f_c', σ_j, and $\tau_1$are expressed in MPa. The expression accounts for the beneficial influence of column axial compression on diagonal cracking of the joint panel (Shin and LaFave 2004; Grande et al. 2021b). The peak joint shear stress was evaluated using the simplified unified model of Kim and LaFave (2012),

$$\tau_{\max} = \lambda_t \alpha_t \beta_t (1 - \frac{e}{b_c})^{0.67} (\frac{\rho_j f_{yj}}{f_c'})^{0.15} (\frac{\rho_b f_{yb}}{f_c'})^{0.30} (f_c')^{0.75} \quad (9)$$

where ρ_j and f_{yj} were the volumetric ratio and yield strength of the joint transverse reinforcement, respectively; ρ_b and f_{yb} were the beam longitudinal reinforcement ratio and yield strength, respectively, for the loading direction considered; e is the joint eccentricity, define as the magnitude of the transverse offset between the beam centerline and the column centroid in plan; and b_c is the column width measured perpendicular to the plane of the frame under consideration. The adjustment coefficient was taken as $\lambda_t = 1.31$; the in-plane geometry coefficient was taken as $\alpha_t = 1.0$, 0.70, and 0.40 for interior, exterior, and knee joints, respectively; and the out-of-plane coefficient was taken as $\beta_t = 1.0$ for zero or one transverse beam and 1.2 for two transverse beams. Equation (9) was developed by Kim and LaFave (2012) from a database of 341 cyclic beam–column connection tests and explicitly distinguishes the influence of in-plane geometry, transverse framing, and joint eccentricity. The remaining stress coordinates of the backbone were defined following the experimentally calibrated model of Shin and LaFave (2004),

$$\tau_2 = 0.90\tau_{\max} \quad (10a)$$

$$\tau_3 = \tau_{\max} \quad (10b)$$

$$\tau_4 = 0.30\tau_{\max} \quad (10c)$$

The corresponding strain coordinates $\gamma_1$through $\gamma_4$were initialized from the ranges reported by Shin and LaFave (2004) and subsequently calibrated against the component-level joint hysteresis. This calibration was retained rather than adopting parameter sets developed for unreinforced or non-code compliant joints, which would overstate joint softening for the confined connections in the subassembly and shake table specimens used for calibration and validation of the modeling approach. The selected stress ratios are consistent with the backbone evaluated by Grande et al. (2021a, b).

The shear stress–strain backbone was transformed into the corresponding spring moment–rotation relation by equilibrium of the exterior-joint free body. At each backbone point,

$$\theta_{j,i} = \gamma_i, M_{j,i} = \frac{\tau_i A_j}{\frac{1-h_c/(2L_b)}{z_{b,i}} - \frac{1}{L_c}} \quad (11)$$

where L_b was the effective beam shear span measured from the joint centerline to the beam inflection point, L_c was the distance between the upper and lower column inflection points, and $z_{b,i}$ was the beam internal lever arm, approximated as the distance between the centroids of the top and bottom longitudinal reinforcement layers and was held constant when constructing the joint spring backbone. Equation (11) is the exterior-joint equilibrium transformation used in the Grande et al. (2021a, b) macro-model, with the joint shear strain taken equal to the scissors-spring rotation.

The connection at the roof of a building does not contain an upper column and is therefore geometrically different from an intermediate-story exterior joint. For consistency within the building model, the same exterior-joint constitutive law was retained as a simplifying assumption, while the upper column arm was removed. Equation (11) was consequently modified by replacing $L_c$with $L_{c,r}$, the distance from the roof joint center to the inflection point in the lower column. This representation is not intended to reproduce a distinct knee-joint failure mechanism. It provides a consistent estimate of roof-joint flexibility while retaining the lower-column contribution to joint shear.

3 CALIBRATION OF MODELING APPROACH AGAINST SUBASSEMBLY TESTS

The modeling approach was used to simulate the response of five reinforced-concrete subassembly specimens from the literature to calibrate component-level parameters. Wall and slab regions were represented by layered shell elements and beam and column members were represented by fiber-discretized beam elements. Joint-panel shear and bar-slip/strain-penetration springs were included to represent connection deformations. Specimen geometry, reinforcement layout, boundary conditions, material properties, axial loading, and imposed displacement histories were reproduced from the original experimental documentation. The material inputs were derived from the measured concrete and reinforcement properties. Fig. 5 illustrates the experimental configurations and corresponding finite-element idealizations, and Table 1 summarizes the principal specimen properties.

Three benchmark specimens were used to calibrate the member-level response of the wall, beam, and column formulations that were later used in the building model validation.

- Wall WSH6 from Dazio et al. (2009) evaluated the layered-shell formulation under flexure-dominated cyclic wall response, including distributed cracking, boundary-region compression, reinforcement yielding, and cyclic stiffness deterioration (Fig 5a).

- Beam 43 from the Berkeley cyclic-beam program [Popov, Bertero & Krawinkler (1972)] evaluated flexural-hinge response under a relatively high shear-to-moment demand (Fig 5b). The comparison was intended to assess beam flexural behavior rather than a shear-failure mechanism.
- Column C1-1 from Mo and Wang (2000) evaluated column-base flexural hinging under constant axial compression and closely spaced transverse reinforcement (Fig 5c).

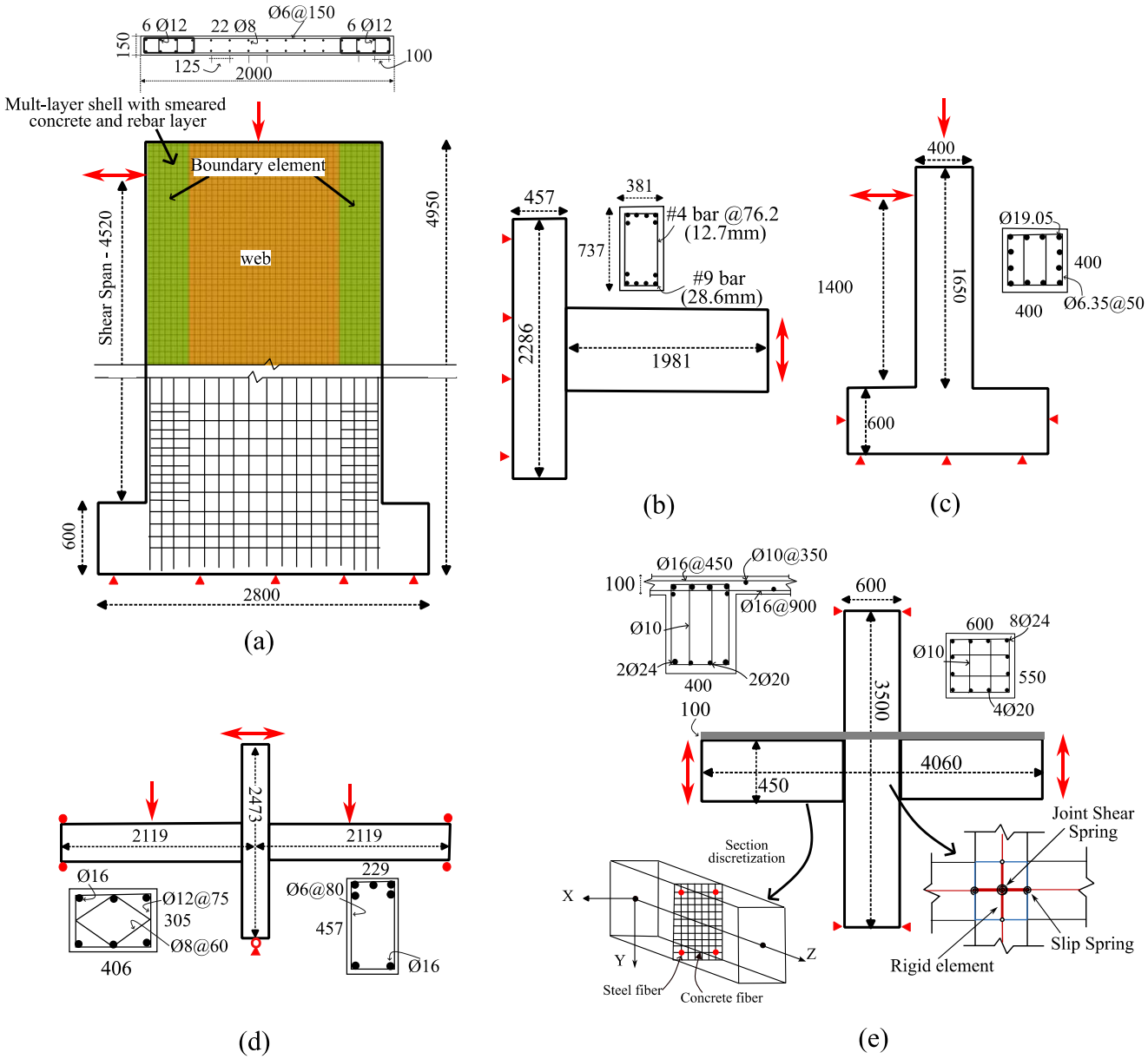


Fig. 5 Geometry, reinforcement details, boundary conditions, and FE idealizations of the five validation subassemblages: (a) WSH6 reinforced-concrete wall; (b) Beam 43 reinforced-concrete beam; (c) C1-1 reinforced-concrete column; (d) Unit 1 beam–column joint; and (e) Unit 1D-I beam–column–slab connection

Two additional specimens evaluated connection-level mechanisms.

- Unit 1 from Park and Dai (1988) was a well-detailed interior beam–column subassembly designed to form plastic hinges in the beams (Fig 5d). It was used to assess whether the combined fiber-member and spring representation reproduces beam hinging, reinforcement slip and strain penetration, and the measured contribution of joint-panel shear deformation without producing an artificial joint failure.

Table 1 Geometric, reinforcement, material, axial-load, and loading characteristics of the five RC subassemblages used for mechanism-level model validation

Parameter	WSH6 (a)	Beam 43 (b)	C1-1 (c)	Unit 1 (d)	Unit 1D-I (e)
Reference	Dazio, Beyer & Bachmann (2009)	Popov, Bertero & Krawinkler (1972), EERC 72-5	Mo & Wang (2000)	Park & Dai (1988)	Cheung, Paulay & Park (1991)
Type / scale	Cantilever wall; ½-scale	Cantilever flexural member (beam); full-size	Cantilever column	Interior beam–column joint; ¾-scale	Interior beam–column–slab joint (1-way); full-scale
Critical section (mm)	2000 × 150	483 × 737 (b × h; d = 641)	400 × 400 col.	col. 406 × 305; beam 229 × 457	col. 600 × 550; beam 400 × 550; slab t = 100
Member length (mm)	L_v = 4520	ℓ = 1981 (cantilever shear span)	L= 1400	H = 2473; beam 2119 each side	beam span 4060; col. 3500
f′c (MPa, cylinder, at test)	45.6	34.7 (14-day)	24.94	45.9	38.0
Longitudinal reinf. (fy, MPa)	boundary 6 Ø12 (584); web 22 Ø8 (576)	6 Ø28.6 (#9) T&B (fy 414; fmax 669)	12 No.6 Ø19.05 (497)	beam Ø16 (294); col. 8Ø16 (498)	beam 4Ø24/2Ø20 (283/300); col. 8Ø24 + 4Ø20 (500/482); slab Ø16 (318)
Transverse reinf. (fy, MPa)	conf. Ø6@50 (519); horiz. Ø6@150	#4 Ø12.7 @76.2 (fy 414; fmax 662)	No.2 Ø6.35 @50 (459.5)	beam Ø6 stirrups; col. Ø12 ties	Ø10 ties
Key reinf. ratio	ρtot = 0.82%; ρbound = 1.54%; ρv = 0.54%; ρh = 0.25%	ρ = ρ′ = 1.58%; ρb (balanced) = 3.36%	ρl ≈ 1.07%	beam ρ = 1.09% / ρ′ = 0.44%; col. ρt = 1.30%	beam ρ ≈ 1.34% (incl. slab); col. ρt = 1.48%
Axial load N (ratio)	1476 kN (N/Agf′c = 0.11)	0	450 kN (≈0.11)	0	0
Loading protocol	QS cyclic, Park (1988), 2 cyc./μ	QS reversed cyclic; load-controlled to yield, then displacement-controlled; 2 cyc./step	QS reversed cyclic; constant N = 450 kN; 0.5% drift increments, 2 cyc./level, to 7.0%	QS reversed cyclic; load-controlled to ±0.75Vth, then displacement-controlled; modeled μ = ±2…±5	QS reversed cyclic; Park-type protocol; modeled μ = ±2…±5; 2 cyc./level

Notes: QS = quasi-static; ρb = balanced longitudinal reinforcement ratio. For Unit 1 and Unit 1D-I, the loading entries report the portion of the experimental history reproduced in the FE comparisons, not the complete test sequence.

- Unit 1D-I from Cheung et al. (1991) was a full-scale, one-way interior beam–column–slab subassembly (Fig 5e). It evaluated the contribution of slab reinforcement to negative beam flexural resistance and the

interaction of slab participation, beam hinging, and joint deformation. Unit 1D-I therefore provides a mechanism-level benchmark for slab participation at the moment-frame connection; it did not constitute direct validation of in-plane diaphragm membrane-force transfer.

Fig. 6 compares the measured and simulated lateral force–displacement histories. The assessment considered initial stiffness, positive and negative peak resistance, the force–deformation envelope, unloading and reloading stiffness, pinching, residual deformation, and cyclic strength and stiffness deterioration. These response characteristics provided a more demanding assessment than peak strength alone because nonlinear, dynamic analyses comprise a sequence of ground motions in which residual deformation, stiffness loss, and accumulated material history affect the subsequent response.

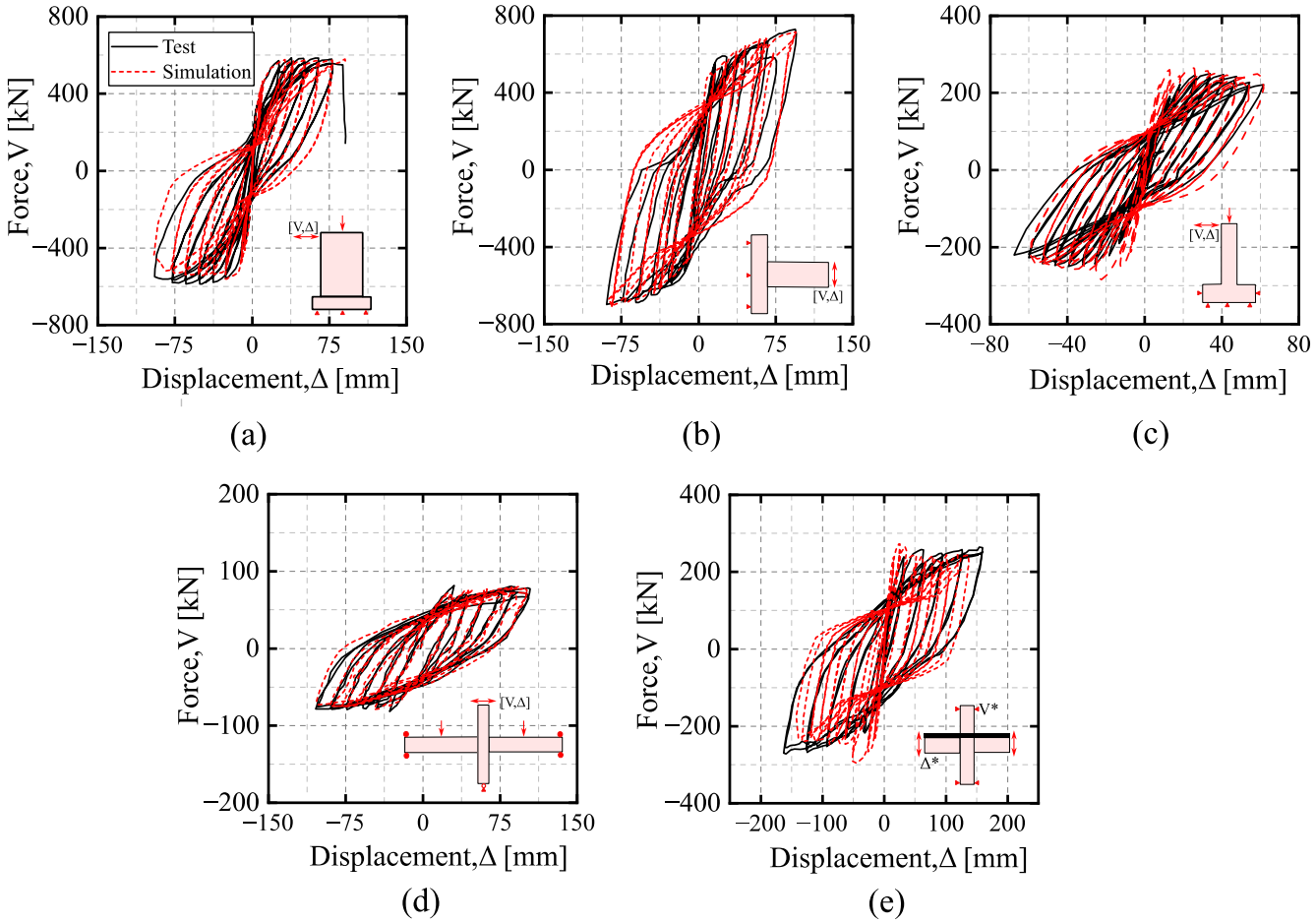


Fig.6 Comparison of measured and simulated cyclic force–displacement responses for the five validation subassemblages: a) WSH6 reinforced-concrete wall; (b) Beam 43 reinforced-concrete beam; (c) C1-1 reinforced-concrete column; (d) Unit 1 beam–column joint; and (e) Unit 1D-I beam–column–slab connection

The comparisons show that the adopted modeling framework reproduced the principal cyclic mechanisms represented in the calibration set: flexure-dominated wall response, beam-end and column-base

hinging, concrete cracking and compression damage, reinforcement yielding, joint-panel flexibility, bar slip and strain penetration, and slab participation in frame flexure. The comparisons did not directly calibrate dynamic strain-rate effects, the geometry-specific response of exterior or roof joints, member shear failure, reinforcement fracture, punching-type slab–column failure, or interaction between diaphragm membrane forces and connection damage. Severe localized failures therefore defined the limits of the calibrated modeling framework rather than mechanisms for which point-by-point damage prediction was possible. Within these limits, the comparisons to the subassembly specimens establish the basis for assembling the complete building model used for validation of the components integrated dynamic response.

4 DESCRIPTION OF 5-STORY RC BUILDING SHAKE TABLE TESTS

The modeling approach was validated against results from shake table tests conducted as part of the Building Nonstructural Components and Systems (BNCS) program at the NEES–UC San Diego Large High-Performance Outdoor Shake Table. This specimen is unique in the experimental literature because the diaphragms in the tested structure contained openings for an elevator shaft and stairs, the performance of which were an important component of the testing program, and the data is well documented and publicly available [Hutchinson et. al. 2012; Pantoli et. al. 2016]. The components of the experimental shake table tests related to the structural system and its performance under earthquake loading are summarized here, for convenience. Details of the complete testing program are provided by Chen et al. (2016).

The full-scale, five-story, CIP RC specimen, shown in Fig. 7, had plan dimensions of 11.0 m × 6.6 m, two bays in the longitudinal direction and one bay in the transverse direction, uniform story height of 4.27 m, and a total structural height of 21.34 m above the foundation, with the longitudinal direction coinciding with the uniaxial shaking direction. The building was designed for high seismic demand representative of a Southern California Site Class D condition using contemporary regional design and construction practice; conceptual performance targets included a peak interstory drift ratio of 2.5% and peak floor accelerations of approximately 0.7 g–0.8 g under design-level shaking (Chen et al. 2016; Pantoli et al. 2013; Ebrahimian et al. 2018). The building was first examined in a base-isolated configuration and subsequently in a fixed-base configuration, for which the isolators were removed and the stiff posttensioned RC foundation was anchored directly to the shake-table platen. The present study focuses on the fixed-base phase because it produced progressively nonlinear structural response and the diaphragm damage of primary interest herein.

The longitudinal lateral-force-resisting system consisted of two moment-resisting frames located along the north and south perimeter lines. The structure contained six 660 mm × 460 mm columns and 300 mm × 710 mm frame beams, with deliberately varied beam reinforcement and connection details over the height,

including high-strength reinforcement at the two lower levels, a post-tensioned hybrid beam system at the third level, ductile connector details at the fourth level, and conventional special moment-frame construction at the fifth level (Chen et al. 2016; Ebrahimian et al. 2018). Of particular relevance to the present investigation, each floor comprised a 200 mm-thick CIP RC flat slab reinforced in both principal directions at the top and bottom surfaces. In addition to smaller service penetrations, each diaphragm contained two major structural openings accommodating the elevator shaft and the stairwell. Two 150 mm-thick RC walls flanking the elevator shaft provided transverse and torsional stiffness. Because these walls were concentrated toward the west side of the plan, the east bay was cross-braced at each level using 32 mm-diameter steel rods to reduce the resulting torsional stiffness imbalance. This combination of large openings, asymmetric vertical resisting elements, flat-slab construction, and floor-specific framing details makes the specimen especially valuable for investigating diaphragm-force redistribution and slab–frame–wall interaction. The bare structure weighed approximately 3010 kN, whereas the fully outfitted building weighed approximately 4420 kN excluding the approximately 1870 kN foundation (Ebrahimian et al. 2018).

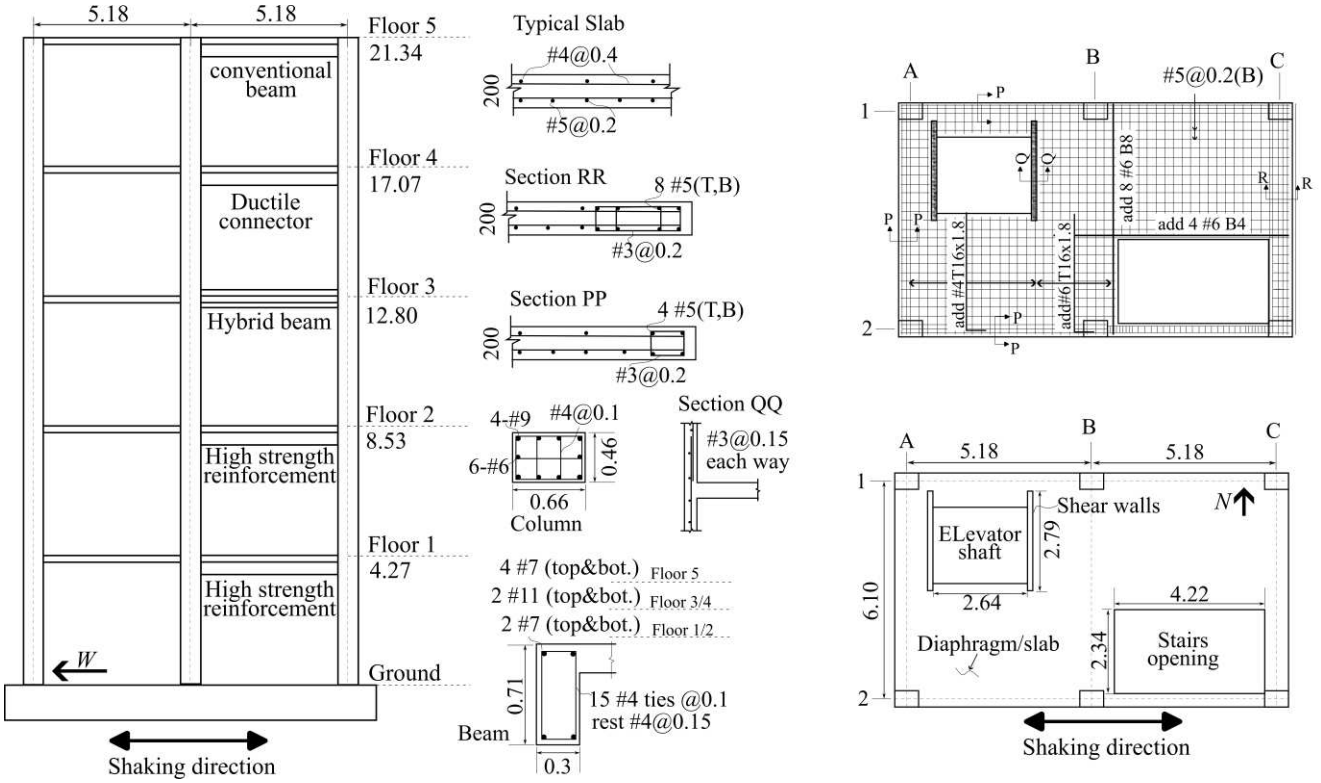


Fig. 7 Structural configuration and diaphragm geometry

The specimen incorporated a broad complement of nonstructural components and systems, of which only the interior partition walls contributed meaningfully to lateral stiffness. Cold-formed-steel-stud/gypsum partition walls were present at all five stories, and their unmodeled stiffness has been identified as the principal source of period and low-amplitude drift discrepancies in pretest simulations, with a diminishing influence as

the partitions progressively cracked at higher shaking intensities (Ebrahimian et al. 2018). The façade systems, precast concrete cladding panels at the upper two stories and a cold-formed-steel balloon-frame façade at the lower three stories, were intentionally detailed with sliding, flexing, and ductile-fuse connections to decouple the cladding from interstory drift and therefore contributed negligible lateral stiffness (Chen et al. 2016; Pantoli et al. 2016).

The specimen was densely instrumented to resolve the response from the global building scale to local member and crack scales, including accelerometers, linear and string potentiometers, LVDTs, reinforcement strain gauges, load cells, GPS receivers, and extensive photographic and video monitoring; more than 600 synchronized data channels were recorded at 240 Hz (Pantoli et al. 2016). Of particular relevance, four triaxial accelerometers were installed near the corners of each floor slab, providing spatially distributed measurement of floor translation and rotation, while local deformation instruments measured beam-end and column-base response, and selected slab-crack opening histories (Pantoli et al. 2016; Ebrahimian et al. 2018). Ambient-vibration and low-amplitude white-noise tests performed at selected stages of the sequence provided independent estimates of the progressive evolution of the building modal properties as damage accumulated (Astroza et al. 2016).

The fixed-base phase comprised six sequential earthquake motions of increasing intensity [Table 2; Fig. 8(a)]. The first two motions, FB1-CNP100 and FB2-LAC100, were spectrally matched serviceability-level motions derived from records of the 1994 Northridge earthquake. These were followed by the ICA record of the 2007 Pisco (Peru) earthquake applied at 50% and 100% scale (FB3-ICA50 and FB4-ICA100). The two strongest tests, FB5-DEN67 and FB6-DEN100, were spectrally matched motions derived from the 2002 Denali TAPS Pump Station 9 record at 67% and 100% scale, representing approximately design-level and maximum-considered-earthquake-level demands, respectively. Measured east-west foundation-level peak accelerations increased from 0.18–0.25g for the first four tests to 0.64g for FB5 and 0.79g for FB6 (Chen *et al.* 2016). As evident from the 5%-damped displacement spectra in Fig. 8(b), the two Denali-derived motions imposed substantially larger long-period deformation demand than the preceding tests and drove the specimen into the strongly nonlinear response range. Because the motions were applied sequentially in the experiment, each test acted on the damage state produced by the preceding motions.

5 VALIDATION OF MODELING APPROACH AGAINST SHAKE TABLE TEST DATA

5.1 Model discretization

Fig. 9 shows the assembled building model, including details of the layered-shell section, fiber-discretized framing members, section offsets, and local beam–slab nodal coupling. The previously defined

shell, fiber-section, and connection representations were assembled into a three-dimensional model of the full five-story BNCS specimen. The model geometry was developed from the as-built structural drawings and reproduced the north and south longitudinal moment frames, the transverse elevator-shaft walls, the cast-in-place floor slabs, the cross bracing, and the principal structural openings.

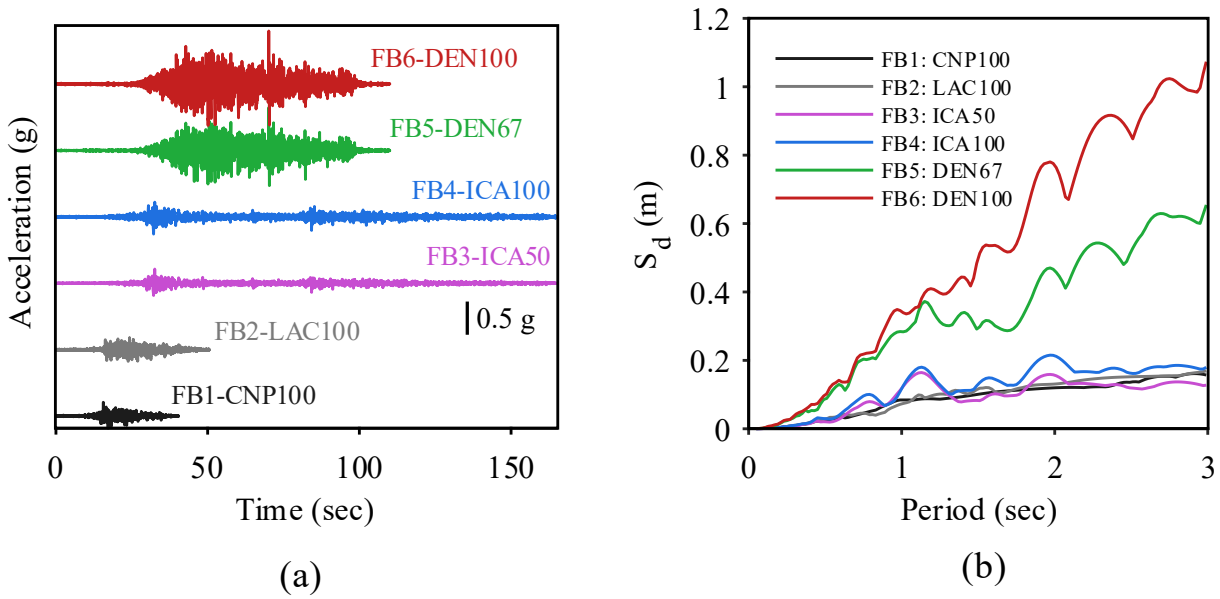


Fig. 8 Earthquake input motions for the fixed-base tests: (a) acceleration time histories; and (b) corresponding displacement response spectra

Table 2 Fixed-base seismic test sequence

Test	Seed earthquake record	Motion description	Role in sequence	Measured PGA (g)
FB1-CNP100	1994 Northridge, Canoga Park	Spectrally matched	Serviceability level	0.20
FB2-LAC100	1994 Northridge, LA City Terrace	Spectrally matched	Serviceability level	0.18
FB3-ICA50	2007 Pisco, ICA	Original record, 50% scale	Intermediate intensity	0.21
FB4-ICA100	2007 Pisco, ICA	Original record, 100% scale	Strong nonlinear response	0.25
FB5-DEN67	2002 Denali, TAPS Pump Station 9	Spectrally matched, 67% scale	Design level	0.64
FB6-DEN100	2002 Denali, TAPS Pump Station 9	Spectrally matched, 100% scale	MCE level	0.79

Note: PGA is the measured east-west foundation-level peak acceleration

The slabs and elevator-shaft walls were discretized using the layered shell formulation described previously. A nominal shell dimension of approximately 100 mm was used in the diaphragm regions examined

for cracking and membrane-force transfer. The slab thickness, reinforcement ratios, reinforcement directions, and vertical positions of the top and bottom reinforcement mats were assigned from the as-built placing drawings as shown in Fig. 7. The elevator and stair openings were represented explicitly by the shell geometry so that force redistribution around the discontinuities developed from equilibrium and compatibility rather than from a predefined chord, collector, or strut-and-tie load path.Columns and frame beams were assigned to the fiber-section formulation established in the preceding section. Member dimensions, confined and unconfined concrete regions, and longitudinal reinforcement layouts were defined separately for each floor. The measured curves of the conventional and high-strength reinforcement, which was used in the first- and second-floor beams, were separately discretized to construct floor-specific constitutive models. The same distinction was used in the corresponding strain-penetration spring backbones, thereby preserving the different yielding and strain-hardening characteristics of the reinforcement installed at the different floors of the building.

The shell and framing meshes were connected while maintaining the physical eccentricity between the slab reference surface and the beam centroidal axis. Section offsets positioned the beam cross sections at their as-built elevations, and shell nodes within the physical beam region were coupled to the corresponding beam nodes using *CONSTRAINED_NODAL_RIGID.

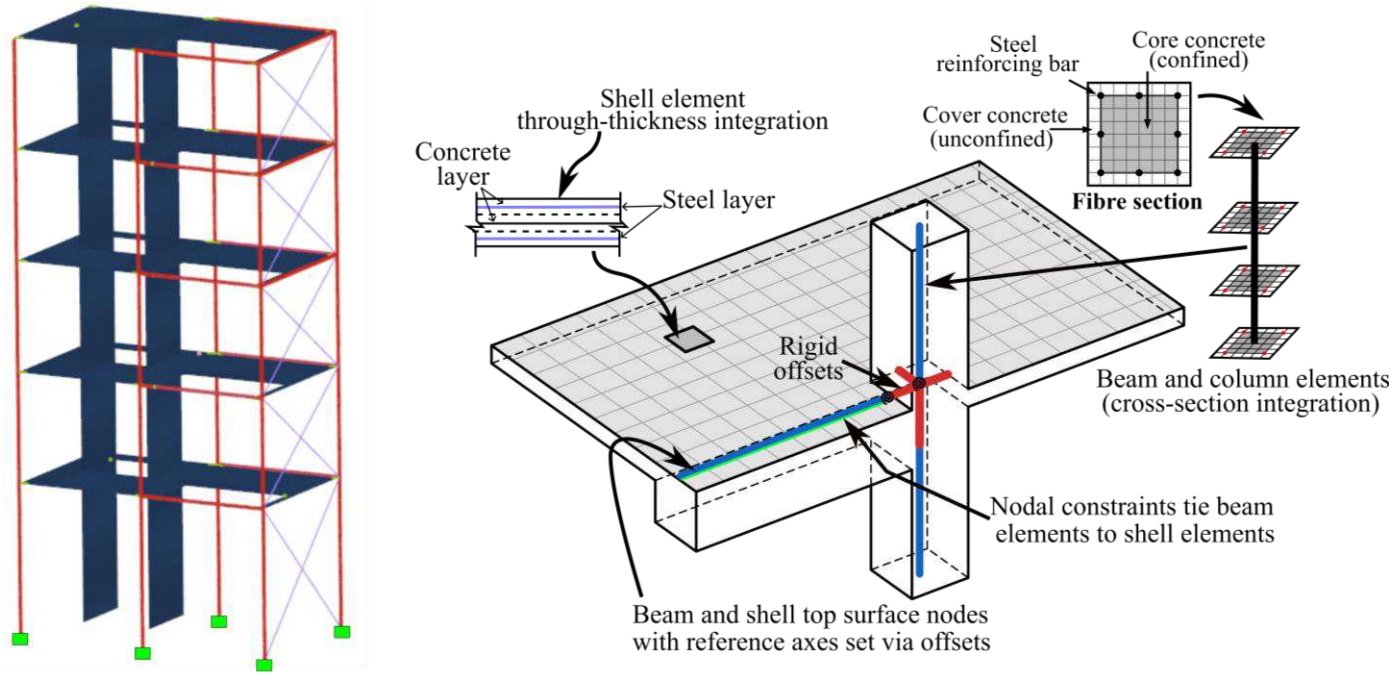


Fig. 9 Modeling strategy for the BNCS building: (a) assembled three-dimensional FE model; and (b) detail modeling tragedy for the specimen

559 At each moment-frame connection, rigid offsets defined the physical joint region, and two-spring
560 representation was inserted to account for joint-panel shear deformation and reinforcement slip/strain
561 penetration. Beam and column flexural deformations remained within the adjoining fiber elements. The
562 connection springs therefore supplemented, rather than replaced, the distributed member response. The same
563 modeling approach that was evaluated in the subassembly test specimen comparisons was retained in the
564 building model, with floor-specific section properties, reinforcement characteristics, and joint parameters
565 assigned to the corresponding BNCS connections.

566 ***5.2 Mass***

567 The model mass comprised the self-mass of the explicitly represented reinforced-concrete members
568 and the added mass of the nonstructural components, systems, and building contents installed during the fixed-
569 base tests. An effective reinforced-concrete bulk density of ρ =2400 kg/m^3 was assigned to the beam, column,
570 slab, and wall elements. The remaining mass; including the façades, partitions, ceilings, stairs, elevator
571 components, distributed mechanical services, roof equipment, and building contents; was represented using
572 lumped-mass definitions associated with node sets and parts. These masses were distributed over tributary floor
573 nodes at the corresponding component plan locations to reproduce the floor mass, center of mass, and mass
574 moment about the vertical axis.

575 The horizontal mass apportionment followed the component-specific rules documented for the BNCS
576 test program and the vertical gravity loads of the non-structural elements were assigned according to their
577 physical support locations (Chen et al. 2013, 2016). The mass of the stair, elevator, and mechanical components
578 were assigned to their corresponding support levels. The elevator cabin and counterweight in their test
579 positions, together with unanchored contents, were treated as unattached and excluded from the horizontal
580 inertia model. The resulting horizontal inertial weight of the five elevated mass levels, including the roof, was
581 approximately 4420 kN.

582 Structural self-weight was applied through *LOAD_BODY_Z and ramped gradually before the first
583 seismic excitation. The model was allowed to equilibrate before the sequence of earthquake motions began.
584 This procedure established the column axial forces, beam and slab gravity demands, and geometric-stiffness
585 and P–Δ effects before the application of the recorded base motions.

586 ***5.3 Energy Dissipation***

587 The principal sources of energy dissipation during strong shaking were represented explicitly through
588 the nonlinear constitutive response, including concrete cracking and crushing, reinforcement yielding and
589 cyclic degradation, joint-panel deformation, and reinforcement slip. Supplemental viscous damping was

introduced only to represent small-amplitude dissipation mechanisms not explicitly resolved by the structural model. Because the NCSs were represented principally through their inertial contribution, their local stiffness, friction, and hysteretic behavior were not modeled explicitly.

Supplemental damping was implemented using *DAMPING_FREQUENCY_RANGE_DEFORM, which applies element-level damping stresses associated with deformational response while avoiding the damping of pure rigid-body motion. A target damping ratio of 3% of critical was specified over the frequency range 0.7–21 Hz. The lower bound was selected slightly below the 0.73-Hz first-mode frequency identified after FB6, while the upper bound encompassed the first three identified longitudinal modes and the higher-frequency structural response relevant to floor accelerations and internal-force demands. The identified longitudinal frequencies decreased from 1.67 Hz, 6.77 Hz, and 10.88 Hz at the beginning of FB1 to 0.73 Hz, 3.70 Hz, and 6.78 Hz at the end of FB6, respectively (Astroza et al. 2019). The selected 30:1 frequency interval remains within the recommended range for the formulation, although the specified ratio is an approximately frequency-independent target and the formulation can slightly modify the dynamic stiffness (LST 2023).

The frequency-range formulation was selected instead of conventional Rayleigh damping because Rayleigh damping varies with modal frequency and can generate unintended forces when its stiffness-proportional component is based on the initial elastic stiffness of a substantially softened structure (Hall 2006; Charney 2008; Chopra and McKenna 2016). The present element-based formulation reduces the sensitivity to two selected Rayleigh anchor frequencies, avoids damping the prescribed rigid-body base motion, and reduces the tendency to overdamp highly softened regions. The adopted 3% ratio is lower than the equivalent first-mode damping identified from the experiments-approximately 5–7% during FB1–FB4, 8% during FB5, and 10% during FB6-because those experimentally identified values incorporate all sources of energy dissipation, including the hysteretic mechanisms represented explicitly in the model (Astroza et al. 2019).

5.4 Base Excitation

Measured foundation-level acceleration histories were applied at the support nodes for each fixed-base test. Motions FB1-FB5 were analyzed independently, each starting from the same gravity-equilibrated state with unchanged model parameters, so that the comparisons through FB5 evaluate a single numerical model over increasing intensities. This choice avoids accumulating numerical error over the lower-intensity motions, during which the experimental damage was limited relative to that produced by FB5.

FB6 was treated differently because FB5 produced substantial cracking, reinforcement yielding, residual deformation, and stiffness loss in the specimen. After the FB5 record ended, the base acceleration was held at zero for 30 s to allow free vibration to decay. The terminal state was written using

*DATABASE_BINARY_D3DUMP, and FB6 was initialized from it with *RESTART_FULL, which transfers the deformed configuration and the constitutive-history variables. FB6 was therefore applied to a model that retained the damage produced during FB5.

6 RESULTS

6.1 Story-Level Response Histories

Fig. 10 compares the measured and simulated interstory drift histories for the second story, where the peak interstory was observed during testing. Three motions are compared, spanning the full intensity range in the experimental program: the serviceability-level (FB1), the design-level (FB5), and the MCE-level test (FB6).

At the serviceability level, shown in Fig. 10a, the simulation reproduced the onset and duration of the strong-response window but overpredicted the 2nd-story drift ratio in both directions. Two differences account for this. First, the simulated response oscillates at a longer predominant period, consistent with the omitted in-plane stiffness of the partition walls, which were undamaged at this stage. Second, the simulated response decays more slowly after the ground motion, whereas the measured response has largely subsided by 20 s. This second observation is attributed to the damping model. A viscous damping of 3% was specified, lower than the 5–7% identified experimentally, because the identified value includes hysteretic dissipation that the constitutive models represent explicitly. At FB1 the structure remains essentially elastic, so little of the identified damping is hysteretic, and the specified ratio underestimates the total dissipation. This discrepancy decreases at higher intensities, as hysteresis becomes the dominant dissipation mechanism.

At the design level, shown in Fig. 10b, the simulated history follows the measured history closely in amplitude and phase through the strong-motion window. The simulated peak drift ratios are 2.91% and 2.16% in the positive and negative directions, compared with measured values of 2.75% and 2.29%, respectively, a difference of about 6% in each direction. This agreement is obtained although the model entered FB5 undamaged, whereas the specimen had already sustained four motions. It indicates that the cracking developed in the early cycles of FB5 brings the model close to the effective stiffness of the specimen, and that damage from the preceding lower-intensity motions has a secondary influence on the design-level response. This observation supports the independent analysis of FB1–FB5; it does not extend to FB6, which follows the substantial damage produced by FB5.

At the MCE level, shown in Fig. 10c, the measured and simulated peak second-story drift ratios are 5.9% and 6.3%, respectively, a difference of about 7%, and the simulation follows the measured response through the strongest cycles near $t \approx 45$ s. Beyond approximately 55 s, the simulated response sustains larger

oscillations, including an excursion near 63 s with no measured counterpart. This divergence follows the fracture of longitudinal reinforcement at the frame-beam ends in the specimen, a limit state not represented in the reinforcement model, and the later portion of the record is therefore not used to assess the model. The divergence occurs after the peak-demand cycles rather than during them, and the instants at which diaphragm quantities are extracted in the following sections (t = 31–45 s for FB5 and t = 45.5 s for FB6) lie within the interval in which the simulation follows the measurement.

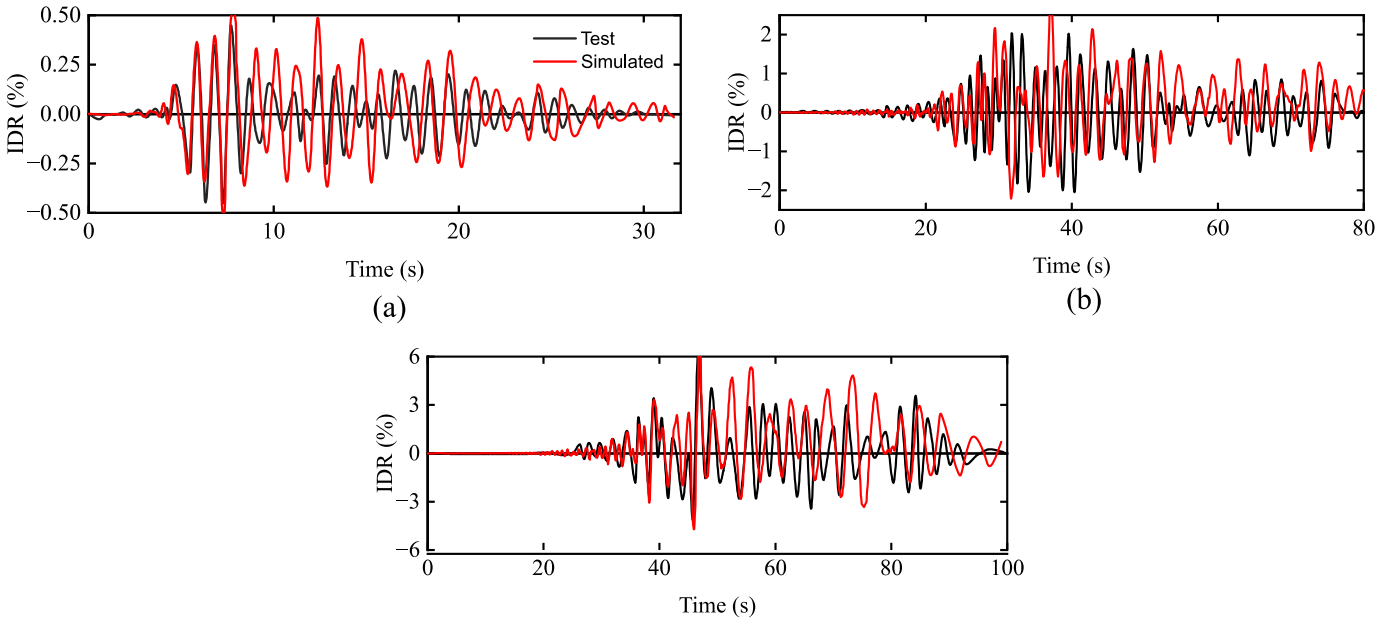


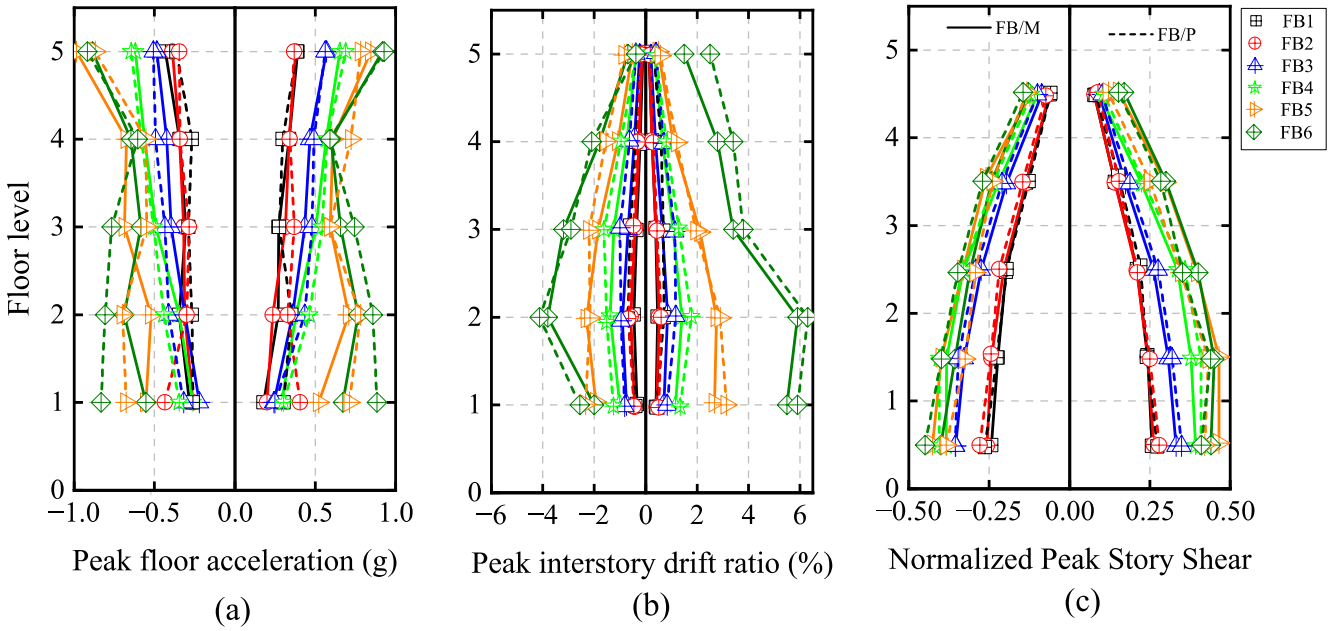
Fig. 10 Measured and simulated second-story interstory drift histories for (a) FB1-CNP100, (b) FB5-DEN67, and (c) FB6-DEN100

6.2 Peak Response Quantities

Simulated and measured peak responses over the height of the building, were compared to assess the system-level accuracy of the model for all six fixed-base motions. Three quantities were compared, relevant to force demands in the diaphragms: the peak floor absolute acceleration (PFAA), which sets the inertial force generated at each floor; the peak total story shear (PTSS), which measures the force transferred through each story and is normalized by the total seismic weight of the specimen; and the peak interstory drift ratio (PIDR), which measures the deformation imposed on the lateral system. The measured floor acceleration at each level was obtained from the four-corner accelerometer array. For the numerical results, acceleration histories were extracted at the six slab–column nodes at each floor. Isolated spikes were removed using a Hampel filter, followed by a fourth-order, zero-phase Butterworth low-pass filter with a cutoff frequency of 25 Hz (over double the third natural frequency of the undamaged building). Drifts were calculated from four-corner-

672 averaged floor displacements relative to the base. This processing was consistent with what was done for the
673 measured data (Hutchinson *et. al.* 2012), to enable direct comparison.

674 Fig 11 compares the measured and simulated PFAA, PIDR, and normalized PTSS envelopes over the
675 building height. The model reproduced the principal features of the measured response across the full range of
676 excitation intensities, including the reduction of floor acceleration through the intermediate levels and its
677 amplification at the roof, the concentration of drift demand in the lower two stories as the response became
678 strongly inelastic, and the systematic decrease of story shear with height. The model also captured the
679 pronounced directional asymmetry of the FB6 drift profile.



680

681 **Fig. 11** Measured (FB/M) and simulated (FB/P) signed peak-response profiles distributions for the six
682 fixed-base motions: (a) peak floor absolute acceleration; (b) peak interstory drift ratio; and (c) peak total story
683 shear normalized by the total seismic weight

684 The measured and simulated quantities were compared for each motion and floor at both positive and
685 negative peaks, giving 60 points of comparison per quantity (=5 floors×6 motions×2 directions). Normalized
686 story shear was predicted best, with a median error of 7% and with 72% of the 60 points within 10% of the
687 measured values and 98% within 20%. Separating the errors by motions, the medians varied only between 5%
688 and 12% from FB1 to FB6, suggesting that the accuracy was essentially independent of intensity. The floor
689 accelerations followed, with a median error of 11% and with 43% of the predicted points within 10% and 68%
690 within 20%. Lastly, the median error for IDR was 15%, with 22% of comparisons within 10% and 55% within
691 20%. The largest absolute errors occur in the strongest motions at the stories of peak inelastic demand, where

the response is most sensitive to the accumulation of inelastic deformation and damage. The largest errors, as a percent of the measured drift, was at the upper stories at low intensity (FB1), where the measured drifts were only 0.1–0.4%. This difference is attributed to the omitted stiffness of the interior partition walls, whose contribution is largest while those components remain undamaged and diminishes as they degrade during stronger motions (Astroza et al. 2016). More broadly, the agreement in the profiles shows that the model was capable of reproducing not only the magnitude of the response but also its distribution over the height of the building across a range of earthquake intensities.

6.3 ***Observed Damage***

The observed frame response was consistent with the intended nonlinear mechanism of the special moment-frame system: flexural hinging developed at the first-story column bases and at the frame beam ends of the lower stories, accompanied at the strongest motions by cover spalling at the hinge regions and, during FB6, fracture of longitudinal reinforcement at several beam ends (Chen et al. 2016; Pantoli et al. 2013). The diaphragm, in contrast, was not intended as a location of inelastic deformation and damage. Slab cracking initiated at the first floor near the north-central and south-central columns at low-to-moderate intensity, propagated around columns, openings, and penetrations through FB4, and by the end of the design-level FB5 motion-which produced peak interstory drift ratios of approximately 2.8% in the lower stories-exhibited dense cracking around the northwest, north-central, south-central, and southwest column regions interpreted in the test documentation as indicating punching-shear distress (Pantoli et al. 2013). During FB6, through-thickness punching damage developed at first-floor slab-column regions, and second-floor cracking concentrated near the stair opening and the central columns, extending approximately 1 m from the south-central column at 200 mm–300 mm spacing (Pantoli et al. 2013). This concentration of slab damage around slab-column connections and floor openings, precisely where the diaphragm load path must transfer into vertical elements of the building, motivates the diaphragm-focused validation and force-transfer investigation presented in this paper.

The BNCS instrumentation did not include strain gauges on the slab reinforcement, so the primary experimental record of diaphragm-level damage is the set of crack maps documented on the top surface of the slabs during the post-test inspections, supplemented by photographs and local crack-width and spacing measurements. Fig. 12 compares these observations against the simulated crack fields at two intensities and two floor levels: the first elevated floor slab after FB5 and the first and second elevated floor slabs after FB6. These correspond to the second and third floor slabs in the test documentation, which numbered levels starting with Floor 1 at the top of the foundation. The observed maps were reconstructed from the inspection records as damage regions rather than individual crack traces: hatching denotes the extent of concentrated slab

cracking, filled markers (red) locate flexural hinging in the frame beams, and star symbols distinguish regions of punching-type damage at the slab–column connections. The simulated crack maps show normalized equivalent crack openings at the top integration points of the layered slab shells. Equivalent openings were calculated by multiplying the nonnegative crack-related strain measure by a characteristic length of 100 mm and then normalized by a reference opening of 1.432 mm, corresponding to the 99th percentile of the calculated openings in the reference dataset. Normalized values exceeding 1 were capped at 1 for visualization. Because the experimental maps record cumulative damage states and the smeared-crack formulation distributes each physical crack over a band of elements, the comparison addresses the location and spatial extent of cracking rather than the geometry or width of individual cracks.

At the design-level motion, the simulated field localizes the cracking at the interior slab–column connections along the moment-frame lines, most strongly at the north-central connection (B1), while the slab interior and the regions immediately surrounding the two openings remain lightly cracked. The post-FB5 inspection records the same discrimination, reporting propagating slab cracking concentrated around the south-central, northwest, north-central, and southwest column regions and interpreting it as punching-shear failure, with the remainder of the floor comparatively intact.

At the MCE level, both the observation and the simulation show expansion and intensification of the same damaged regions rather than the emergence of new ones. The inspection after FB6 reports cracking extending through the full slab thickness at the northwest, north-central, and northeast connections and identifies punching-shear failure at the north-central and northwest locations; these are the three regions carrying the strongest simulated crack-opening concentrations in Fig. 12(d), and the crack field elsewhere spreads along the column lines and along a band extending from the stair opening.

Both the measured and the simulated crack maps show the development of an elongated band of damage running diagonally through the slab between the elevator and stair openings and terminating at the south-central connection (B2). It was observed after FB5 (Fig. 12a) and developed into one of the most extensive damaged features of the floor by FB6 (Fig. 12c). The simulation reproduced the position, orientation, and growth of this damage between the two intensities. Unlike other regions of damage, this pattern cannot be fully attributed to connection flexure. The damaged region occupied the narrowest continuous slab region on the floor, through which the in-plane forces flowed, interrupted from a more direct path to the frame lines by the two large openings. The damage region terminated where forces could be delivered to the moment frame, and its geometry is that of a diagonal strut, with transverse tension cracking occurring in the slab along an inclined compression trajectory anchored at B2.

At the MCE level, inspection records revealed concentrated cracking at the northwest re-entrant corner of the stair opening (Fig. 12e), alongside closely spaced cracking between the frame lines east of the opening. Re-entrant corner distress is the classical consequence of a geometric discontinuity in a loaded membrane: the force path must turn abruptly and the stress field concentrates at the corner, while the stress in the surrounding slab is comparatively reduced. The simulated field develops a discrete concentration at the same corner (Fig. 12f), over a smaller area than the inspection recorded, largely a consequence of the resulting stress singularity, the smeared-crack band model, and the mesh size.

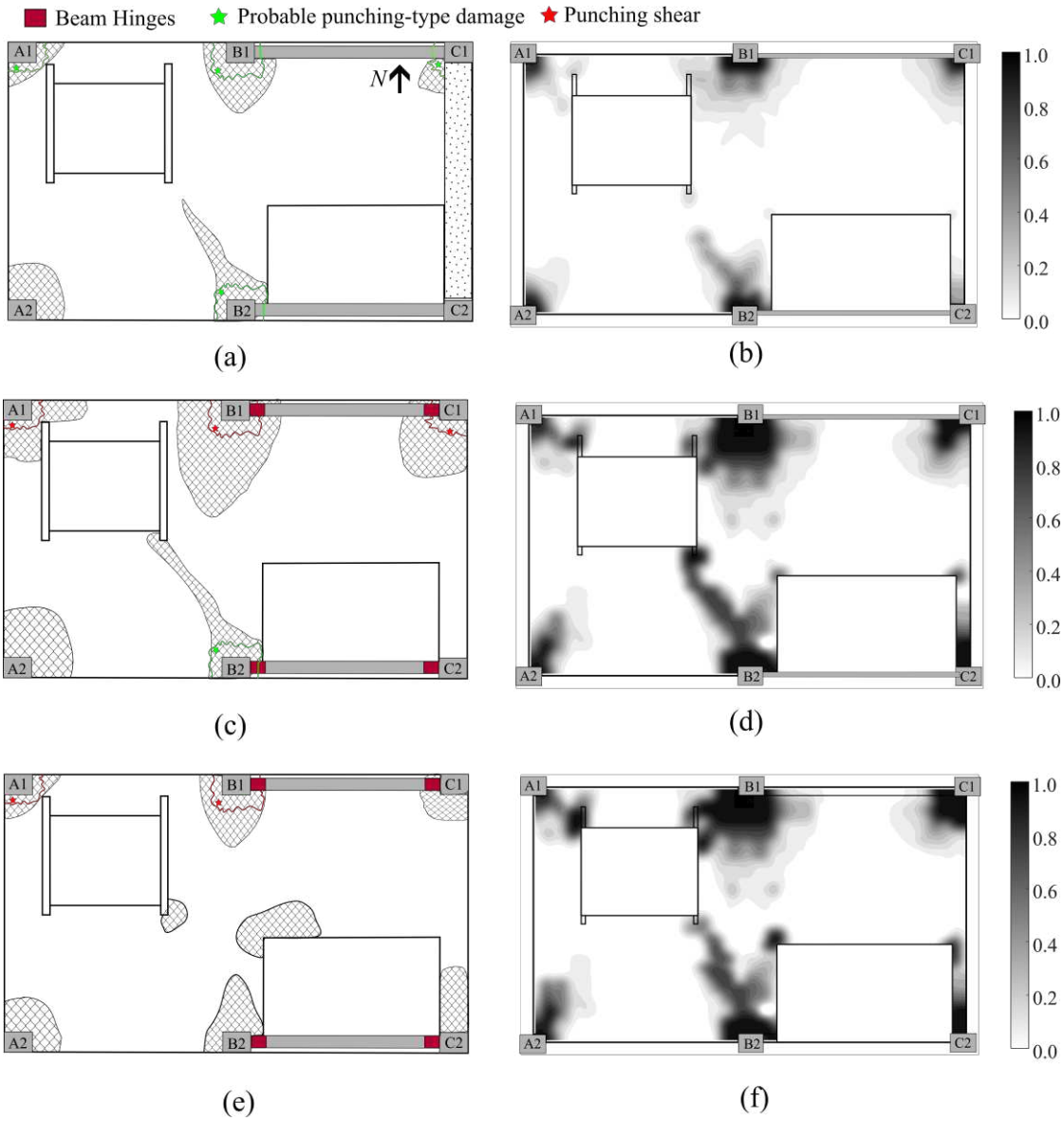


Fig. 12 Observed and simulated top-surface slab cracking for (a,b) First floor after FB5-DEN67, (c,d) Second Floor after FB6-DEN100, and (e,f) Floor 2 after FB6-DEN100

Comparisons with the remaining local measurements, including floor rotations from the corner accelerometers, beam and slab elongations, selected slab-crack opening histories, and reinforcement strains in

the frame members, showed agreement consistent with the comparisons presented here and are not reported for brevity. Diaphragm membrane forces, in contrast, were not measured in the test and cannot be obtained directly from shake-table data. The model reproduces both the global response, which sets the total force each floor must carry, and the local slab damage, which shows where that force travels; the membrane forces between these two levels are therefore constrained by validated quantities at both ends.

6.4 In-plane Diaphragm Forces

Membrane resultants N_x, N_y, and N_{xy} were extracted from the layered shells and transformed from element-local coordinates to the global floor axes, with x parallel to the shaking direction and y transverse to it. These quantities represent forces per unit width integrated through the slab section, with tension positive. The principal resultants, N_1 and N_2, were calculated from the membrane values, with $N_1 \geq N_2$.

Four configurations were selected for each motion: the positive and negative peaks of the floor force ($F_{px}+$, $F_{px}-$) and of the first-story drift (PIDR+, PIDR−). Fig. 13 compares FB1, FB5, and FB6 at $F_{px}-$, which corresponds to the largest absolute floor force for each of these motions. Fig. 14 shows the remaining three configurations for FB5. All contours use a common ±850 N/mm scale. Slab regions within one slab thickness (200 mm) of the column faces are masked to improve visualization of the surrounding force field. Several features of diaphragm response can be observed from these figures:

- ***The force distribution changed with shaking intensity.*** At peak negative ($F_{px}-$), tensile demand during FB1 was concentrated near the north-central connection, B1. During FB5 and FB6, the tensile region extended from the elevator opening across the slab north of the stair opening (Fig. 13). Compression remained concentrated along narrower bands, particularly north of the stair opening and along parts of the northern perimeter. The stronger motions therefore increased the force magnitudes and engaged a larger area in tension. This change is consistent with redistribution as cracking and inelastic deformation altered the stiffness of the slab and the vertical system.

- ***Different response states engaged different regions of the slab.*** During FB5, peak positive floor acceleration ($F_{px}+$) produced a tensile band extending from the vicinity of B2 toward the northwest corner of the stair opening (Fig. 14). At peak negative drift, tension spread more broadly across the slab east of the elevator opening. At peak positive drift, this broad tensile region was less pronounced, while demand remained concentrated near the central ligament and B1. The two drift directions did not produce mirrored force patterns. Thus, it is observed that one global-response peak may not represent all the force distributions developed within the diaphragm.

- ***The slab developed several membrane-force states.*** Regions of biaxial tension (TT), tension–compression (TC), and biaxial compression (CC) occurred within the same diaphragm (Figs. 13 and 14), whereas the equivalent-beam idealization assumes pure shear throughout the slab between the chords. At peak negative (F_{px}−), the TT area increased from approximately 8% in FB1 to 19% in FB5 and 25% in FB6. Over the same states, the area below the specified demand threshold decreased from 45% to approximately 4% and 2%. These results show that more of the slab participated in carrying membrane forces during the stronger motions.

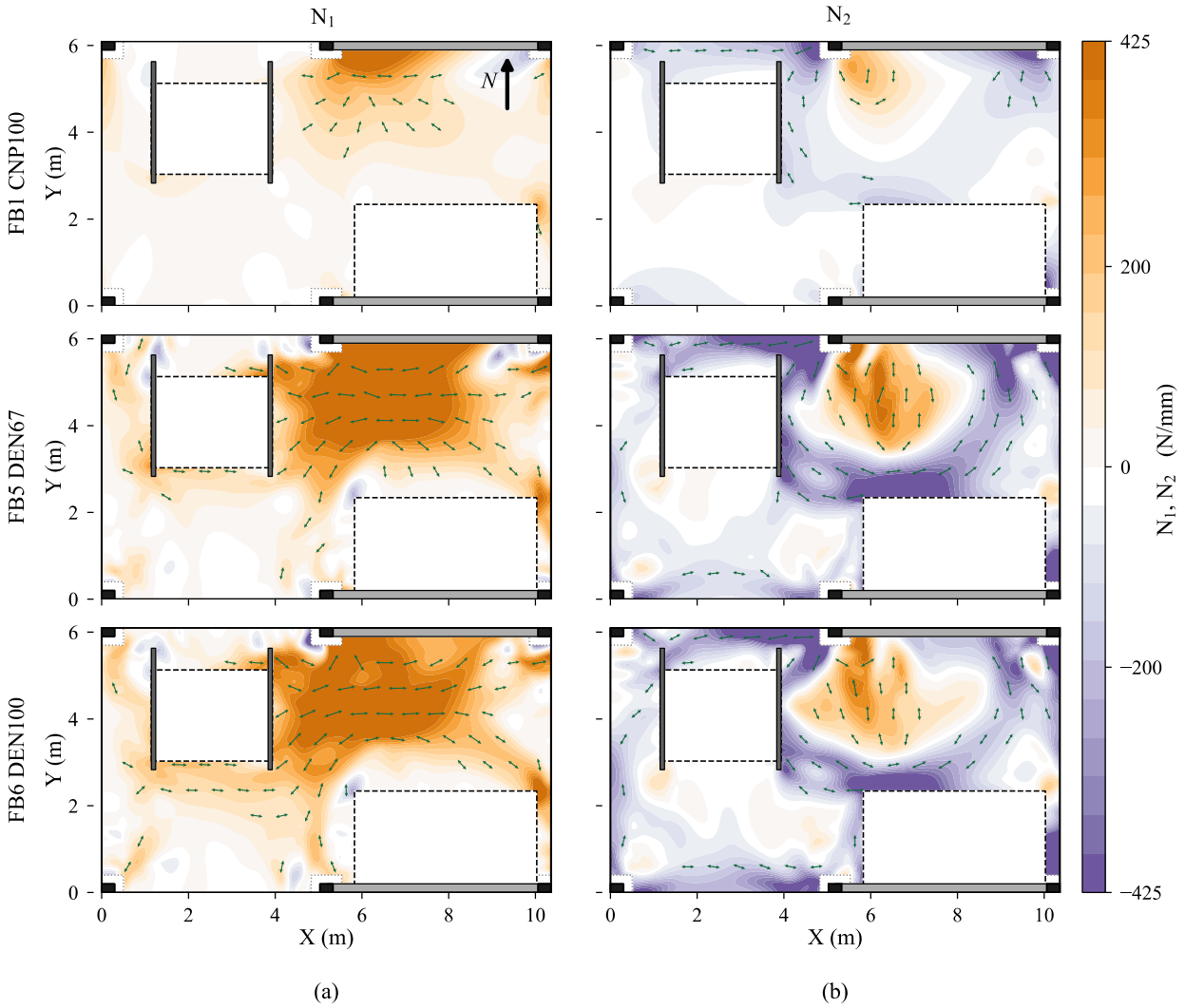


Fig. 13 Principal membrane resultants in the first-floor diaphragm at peak negative floor force: (a) N_1; and (b) N_2

- **Tension became more widely distributed, while compression remained localized.** At peak negative (F_{px}−), the area containing half of the area-integrated tensile demand,A50, increased from approximately 11% in FB1 to 17% in FB5 and 19% in FB6. The corresponding compression measure remained within a relatively narrow range. Even during the stronger motions, the force distribution was therefore far from uniform.

These results can guide future studies of small and intermediate openings. Portions of the southwestern slab interior carried comparatively smaller membrane forces in the displayed configurations and could be examined as candidate locations. However, a lightly loaded region at one instant may carry larger forces at another. Candidate locations should therefore be assessed across the response history. Also, TT, TC, and CC classifications describe the local force state; they do not by themselves establish where an opening can be permitted.

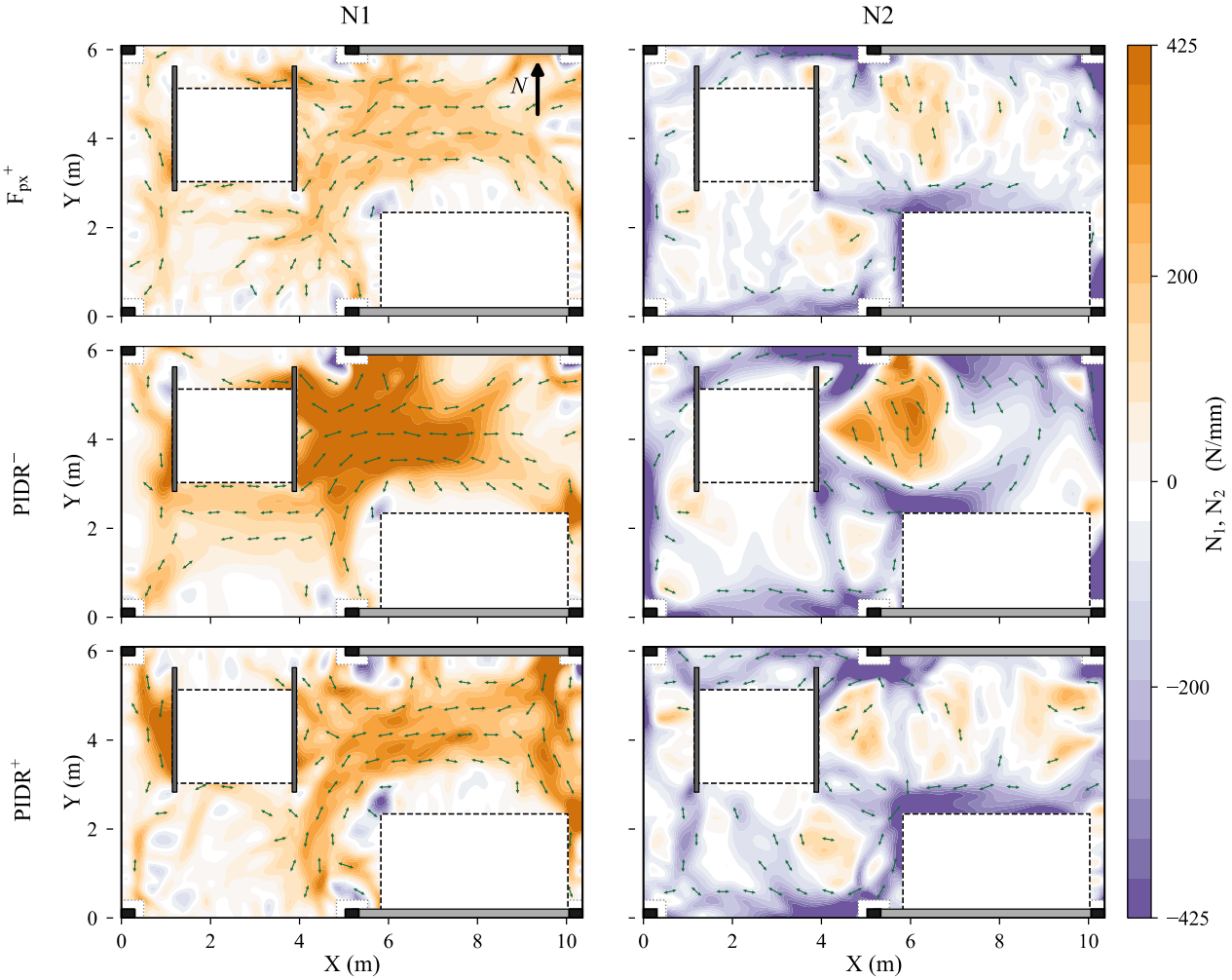


Fig. 14 Response-state dependence of the FB5-DEN67 principal membrane resultants in the first-floor diaphragm: (a) N1; and (b) N2

7 SUMMARY AND CONCLUSIONS

To study the response and design of CIP diaphragms with openings, a modeling framework was developed, capable of both reproducing the dynamic force arriving at the diaphragm level and resolving the load path through the slab with high fidelity. The present study calibrated and validated this computationally efficient three-dimensional diaphragm modeling framework in LS-DYNA. The approach used nonlinear

layered-shells for the wall and diaphragm elements and fiber-based beam-column elements for frame components, providing a deliberate intermediate level of resolution: the approach preserved the dynamic interaction of the complete building while resolving the distributed slab membrane resultants needed to interrogate the diaphragm force path.

Components of the modeling strategy were first calibrated against the results from cyclic beam-column and wall subassemblies, and the assembled building model was then validated against shake table tests of a multistory reinforced concrete building model, which contained slab openings. The component calibration establishes whether the adopted element formulations, constitutive models, and connection idealizations reproduce the principal cyclic mechanisms before they are combined; the building-level validation then tests whether their interaction reproduces the measured system response and the observed slab damage. The performance of the modeling approach was assessed using measured floor accelerations, interstory drifts, story shears, local member and connection deformations, and observed slab-damage regions. The experimentally validated framework provided a direct link between global building response, distributed diaphragm mechanics, and the localized regions in which damage was observed. Highly localized damage mechanisms such as slab-column connection punching and bar fracture were not explicitly modeled and are recognized as a limitation of the reduced-order modeling approach.

The diaphragm-force analysis, based on a limited set of computationally demanding full-building simulations, led to the following findings:

- During the stronger motions, tensile demand spread over larger slab areas, while compression remained concentrated in narrower regions. These changes in the diaphragm load path are consistent with stiffness changes caused by progressive cracking and inelastic deformation of the diaphragm and vertical elements of the lateral force resisting system.

- The diaphragm load path varied with the response instant. Force distributions at peak floor force differed from those at peak interstory drift, and the positive and negative peaks engaged different slab regions. Regions carrying substantial demand at one instant could unload at another. A single peak-response configuration therefore does not describe the evolving diaphragm load path.

- Biaxial tension, tension–compression, and biaxial compression developed within the same diaphragm under unidirectional shaking. The extent of these regions changed with the motion and response instant, showing that the direction of excitation alone does not describe the local membrane-force state around openings. Examining these states together with the force magnitudes may help identify suitable regions for

small and intermediate openings. Further study is needed to assess demand throughout the response history and the redistribution caused by introducing each opening.

Because the diaphragm is represented as a continuous nonlinear slab within the full building model, the modeling approach can resolve the inertial force path through the structural system, including (1) the net inertial force developed at each floor, which can be compared directly with code diaphragm design forces; (2) the distribution and redistribution of membrane forces around openings, including chord- and collector-type actions; and (3) the multiaxial forces transferred across slab–LFRS connection regions. Extending the approach to building archetypes with other floor plans, opening configurations, and LFRS types would allow the risk of CIP diaphragm damage, and its implications for resilience and functional recovery, to be quantified. Such studies would also identify where conventional diaphragm idealizations remain adequate and where opening-induced redistribution and nonlinear interaction with the vertical system produce demands that elastic design forces do not capture. The modeling approach therefore provides a basis for diaphragm design procedures informed by explicitly computed demands rather than implicit idealizations.

8 REFERENCES

ACI Committee 374 (2016) Guide to nonlinear modeling parameters for earthquake-resistant structures (ACI 374.3R-16). American Concrete Institute, Farmington Hills, MI

Al Harash MT (2011) Inelastic seismic response of reinforced concrete buildings with floor diaphragm openings. Dissertation, Washington University in St. Louis. https://doi.org/10.7936/K71834KQ

Alath S, Kunnath SK (1995) Modeling inelastic shear deformation in RC beam–column joints. In: Proceedings of the 10th Conference on Engineering Mechanics, vol 2. ASCE, New York, pp 822–825

ASCE (2022) Minimum design loads and associated criteria for buildings and other structures (ASCE/SEI 7-22). American Society of Civil Engineers, Reston, VA. https://doi.org/10.1061/9780784415788

ASME (2020) Standard for verification and validation in computational solid mechanics (ASME V&V 10-2019). American Society of Mechanical Engineers, New York

Astroza R, Ebrahimian H, Conte JP, Restrepo JI, Hutchinson TC (2016) System identification of a full-scale five-story reinforced concrete building tested on the NEES-UCSD shake table. Struct Control Health Monit 23:535–559. https://doi.org/10.1002/stc.1778

Astroza R, Hernández F, Gutiérrez G, Díaz P (2019) Dynamic characterization of a full-scale 5-story R/C seismically damaged building specimen. In: Proceedings of the 12th Canadian Conference on Earthquake Engineering, Quebec City, Canada

Bao Y, Lew HS, Kunnath SK (2014) Modeling of reinforced concrete assemblies under column-removal scenario. J Struct Eng 140:04013026. https://doi.org/10.1061/(ASCE)ST.1943-541X.0000773

Barron JM, Hueste MBD (2004) Diaphragm effects in rectangular reinforced concrete buildings. ACI Struct J 101:615–624. https://doi.org/10.14359/13383

Bažant ZP, Oh BH (1983) Crack band theory for fracture of concrete. Mater Struct 16:155–177. https://doi.org/10.1007/BF02486267

Belytschko T, Lin JI, Tsay C-S (1984) Explicit algorithms for the nonlinear dynamics of shells. Comput Methods Appl Mech Eng 42:225–251. https://doi.org/10.1016/0045-7825(84)90026-4

Bull DK (2004) Understanding the complexities of designing diaphragms in buildings for earthquakes. Bull N Z Soc Earthq Eng 37:70–88. https://doi.org/10.5459/bnzsee.37.2.70-88

Canterbury Earthquakes Royal Commission (2012) Final report, Volume 6: Canterbury Television Building (CTV). Canterbury Earthquakes Royal Commission, Christchurch, New Zealand

CEN (2004a) Eurocode 2: Design of concrete structures – Part 1-2: General rules – Structural fire design (EN 1992-1-2:2004). European Committee for Standardization, Brussels

CEN (2004b) Eurocode 8: Design of structures for earthquake resistance – Part 1: General rules, seismic actions and rules for buildings (EN 1998-1:2004). European Committee for Standardization, Brussels

Charney FA (2008) Unintended consequences of modeling damping in structures. J Struct Eng 134:581–592. https://doi.org/10.1061/(ASCE)0733-9445(2008)134:4(581)

Chen M, Pantoli E, Wang X, Astroza R, Ebrahimian H, Mintz S, Hutchinson T, Conte J, Restrepo J, Meacham B, Kim J, Park H (2013) BNCS Report #1: Full-scale structural and nonstructural building system performance during earthquakes and post-earthquake fire – specimen design, construction, and test protocol. Structural Systems Research Project Report SSRP-13/09, University of California, San Diego, La Jolla, CA

Chen MC, Pantoli E, Wang X, Astroza R, Ebrahimian H, Hutchinson TC, Conte JP, Restrepo JI, Marin C, Walsh KD, Bachman RE, Hoehler MS, Englekirk R, Faghihi M (2016) Full-scale structural and nonstructural building system performance during earthquakes: Part I – Specimen description, test protocol, and structural response. Earthq Spectra 32:737–770. https://doi.org/10.1193/012414EQS016M

Cheung PC, Paulay T, Park R (1991) New Zealand tests on full-scale reinforced concrete beam-column-slab subassemblages designed for earthquake resistance. In: Design of beam-column joints for seismic resistance (ACI SP-123). American Concrete Institute, Detroit, MI, pp 1–38. https://doi.org/10.14359/10258

Chopra AK, McKenna F (2016) Modeling viscous damping in nonlinear response history analysis of buildings for earthquake excitation. Earthq Eng Struct Dyn 45:193–211. https://doi.org/10.1002/eqe.2622

Correal JF, Hidalgo V, Reyes JC, Ángel CC (2020) A comparative study of seismic diaphragm design forces for RC dual system buildings. Bull Earthq Eng 18:4515–4540. https://doi.org/10.1007/s10518-020-00870-8

Dazio A, Beyer K, Bachmann H (2009) Quasi-static cyclic tests and plastic hinge analysis of RC structural walls. Eng Struct 31:1556–1571. https://doi.org/10.1016/j.engstruct.2009.02.018

Dhakal RP, Maekawa K (2002) Modeling for postyield buckling of reinforcement. J Struct Eng 128:1139–1147. https://doi.org/10.1061/(ASCE)0733-9445(2002)128:9(1139)

Dulacska H (1972) Dowel action of reinforcement crossing cracks in concrete. ACI J Proc 69:754–757. https://doi.org/10.14359/11281

Eatherton MR, O'Brien PE, Easterling WS (2020) Examination of ductility and seismic diaphragm design force-reduction factors for steel deck and composite diaphragms. J Struct Eng 146:04020231. https://doi.org/10.1061/(ASCE)ST.1943-541X.0002797

928 Ebrahimian H, Astroza R, Conte JP, Hutchinson TC (2018) Pretest nonlinear finite-element modeling and response
929 simulation of a full-scale five-story reinforced concrete building tested on the NEES-UCSD shake table. J Struct Eng
930 144:04018009. https://doi.org/10.1061/(ASCE)ST.1943-541X.0001963

931 El-Ariss B (2007) Behavior of beams with dowel action. Eng Struct 29:899–903.
932 https://doi.org/10.1016/j.engstruct.2006.07.008

933 fib (2008) Practitioners' guide to finite element modelling of reinforced concrete structures. fib Bulletin 45, International
934 Federation for Structural Concrete, Lausanne.

935 Fischer AW, Schafer BW (2023a) Wall-diaphragm interactions in seismic response of building systems I: Parametric
936 models and elastic response. Earthq Eng Struct Dyn 52:1678–1703. https://doi.org/10.1002/eqe.3836

937 Fischer AW, Schafer BW (2023b) Wall-diaphragm interactions in seismic response of building systems II: Inelastic
938 response and design. Earthq Eng Struct Dyn 52:1557–1577. https://doi.org/10.1002/eqe.3829

939 Fleischman RB, Farrow KT (2001) Dynamic behavior of perimeter lateral-system structures with flexible diaphragms.
940 Earthq Eng Struct Dyn 30:745–763. https://doi.org/10.1002/eqe.36

941 Fleischman RB, Naito CJ, Restrepo J, Sause R, Ghosh SK (2005a) Seismic design methodology for precast concrete
942 diaphragms, Part 1: Design framework. PCI J 50:68–83

943 Fleischman RB, Naito CJ, Restrepo J, Sause R, Ghosh SK, Wan G, Schoettler M, Cao L (2005b) Seismic design
944 methodology for precast concrete diaphragms, Part 2: Research program. PCI J 50:14–31.
945 https://doi.org/10.15554/pcij.11012005.14.31

946 Fleischman RB, Restrepo JI, Naito CJ, Sause R, Zhang D, Schoettler M (2013) Integrated analytical and experimental
947 research to develop a new seismic design methodology for precast concrete diaphragms. J Struct Eng 139:1192–
948 1204. https://doi.org/10.1061/(ASCE)ST.1943-541X.0000734

949 Godínez SE, Restrepo JI (2023) Stringer-panel model to support the seismic design and response verification of building
950 diaphragms. Resilient Cities Struct 2:46–67. https://doi.org/10.1016/j.rcns.2023.02.003

951 Grande E, Imbimbo M, Napoli A, Nitiffi R, Realfonzo R (2021a) A macro-modelling approach for RC beam-column
952 exterior joints: first results on monotonic behaviour. J Build Eng 39:102202.
953 https://doi.org/10.1016/j.jobe.2021.102202

954 Grande E, Imbimbo M, Napoli A, Nitiffi R, Realfonzo R (2021b) A nonlinear macro-model for the analysis of monotonic
955 and cyclic behaviour of exterior RC beam-column joints. Front Mater 8:719716.
956 https://doi.org/10.3389/fmats.2021.719716

957 Hall JF (2006) Problems encountered from the use (or misuse) of Rayleigh damping. Earthq Eng Struct Dyn 35:525–
958 545. https://doi.org/10.1002/eqe.541

959 Hughes TJR, Liu WK (1981) Nonlinear finite element analysis of shells: Part I. Three-dimensional shells. Comput
960 Methods Appl Mech Eng 26:331–362. https://doi.org/10.1016/0045-7825(81)90121-3

961 Hutchinson T, Restrepo J, Conte J, Pantoli E, Chen M, Wang X, Astroza R, Ebrahimian H (2012) Shake table testing of
962 a five story building outfitted with NCSs (BNCS project) [dataset]. DesignSafe-CI.
963 https://doi.org/10.4231/D38W38349

964 Janevski A, Kang J-D, Isaković T (2023) Simulation of the E-Defense 2015 test on a 10-storey building using macro-
965 models. Bull Earthq Eng 21:6553–6584. https://doi.org/10.1007/s10518-023-01734-7

966 Khajehdehi R, Panahshahi N (2016) Effect of openings on in-plane structural behavior of reinforced concrete floor slabs.
967 J Build Eng 7:1–11. https://doi.org/10.1016/j.jobe.2016.04.011

Kim J, LaFave JM (2012) A simplified approach to joint shear behavior prediction of RC beam-column connections. Earthq Spectra 28:1071–1096. https://doi.org/10.1193/1.4000064

Kunnath SK, Panahshahi N, Reinhorn AM (1991) Seismic response of RC buildings with inelastic floor diaphragms. J Struct Eng 117:1218–1237. https://doi.org/10.1061/(ASCE)0733-9445(1991)117:4(1218)

Lowes LN, Altoontash A (2003) Modeling reinforced-concrete beam-column joints subjected to cyclic loading. J Struct Eng 129:1686–1697. https://doi.org/10.1061/(ASCE)0733-9445(2003)129:12(1686)

Lowes LN, Mitra N, Altoontash A (2004) A beam-column joint model for simulating the earthquake response of reinforced concrete frames. PEER Report 2003/10, Pacific Earthquake Engineering Research Center, University of California, Berkeley, CA

LST (2023) LS-DYNA keyword user's manual, Volume II: Material models (LS-DYNA R14). Livermore Software Technology, an Ansys company, Livermore, CA

Mander JB, Priestley MJN, Park R (1988) Theoretical stress-strain model for confined concrete. J Struct Eng 114:1804–1826. https://doi.org/10.1061/(ASCE)0733-9445(1988)114:8(1804)

Mo YL, Wang SJ (2000) Seismic behavior of RC columns with various tie configurations. J Struct Eng 126:1122–1130. https://doi.org/10.1061/(ASCE)0733-9445(2000)126:10(1122)

Moehle JP, Hooper JD, Meyer TR (2016) Seismic design of cast-in-place concrete diaphragms, chords, and collectors: a guide for practicing engineers, 2nd edn. NIST GCR 16-917-42, National Institute of Standards and Technology, Gaithersburg, MD. https://doi.org/10.6028/NIST.GCR.16-917-42

Nebrijo J, Jünemann R, Rossetto T (2026) Collapse probability assessment of mid- and high-rise shear wall buildings under earthquake events: sensitivity to floor flexibility and damping modelling. Bull Earthq Eng 24:971–999. https://doi.org/10.1007/s10518-025-02314-7

Panahshahi N, Reinhorn AM, Kunnath SK, Lu L-W, Huang T, Yu KB (1991) Seismic response of a 1:6 reinforced concrete scale-model structure with flexible floor diaphragms. ACI Struct J 88:315–324

Pantoli E, Chen M, Wang X, Astroza R, Ebrahimian H, Mintz S, Hutchinson T, Conte J, Restrepo J, Meacham B, Kim J, Park H (2013) BNCS Report #2: Full-scale structural and nonstructural building system performance during earthquakes and post-earthquake fire – test results. Structural Systems Research Project Report SSRP-13/10, University of California, San Diego, La Jolla, CA

Pantoli E, Chen MC, Hutchinson TC, Astroza R, Conte JP, Ebrahimian H, Restrepo JI, Wang X (2016) Landmark data set from the Building Nonstructural Components and Systems (BNCS) project. Earthq Spectra 32:1239–1259. https://doi.org/10.1193/100614EQS150

Park R, Dai R (1988) A comparison of the behaviour of reinforced concrete beam-column joints designed for ductility and limited ductility. Bull N Z Natl Soc Earthq Eng 21:255–278. https://doi.org/10.5459/bnzsee.21.4.255-278

Pecce M, Ceroni F, Maddaloni G, Iannuzzella V (2017) Assessment of the in-plane deformability of RC floors with traditional and innovative lightening elements in RC framed and wall structures. Bull Earthq Eng 15:3125–3149. https://doi.org/10.1007/s10518-017-0083-0

Popov EP, Bertero VV, Krawinkler H (1972) Cyclic behavior of three R/C flexural members with high shear. EERC Report No. 72-5, Earthquake Engineering Research Center, University of California, Berkeley, CA

Rodriguez ME, Restrepo JI, Carr AJ (2002) Earthquake-induced floor horizontal accelerations in buildings. Earthq Eng Struct Dyn 31:693–718. https://doi.org/10.1002/eqe.149

Ruggieri S, Porco F, Uva G (2020) A practical approach for estimating the floor deformability in existing RC buildings: evaluation of the effects in the structural response and seismic fragility. Bull Earthq Eng 18:2083–2113. https://doi.org/10.1007/s10518-019-00774-2

Scarry JM (2014) Floor diaphragms – seismic bulwark or Achilles' heel. In: Proceedings of the New Zealand Society for Earthquake Engineering Annual Conference, Auckland, New Zealand, Paper O19

Schoettler MJ, Belleri A, Zhang D, Restrepo JI, Fleischman RB (2009) Preliminary results of the shake-table testing for the development of a diaphragm seismic design methodology. PCI J 54:100–124

Shin M, LaFave JM (2004) Modeling of cyclic joint shear deformation contributions in RC beam-column connections to overall frame behavior. Struct Eng Mech 18:645–669. https://doi.org/10.12989/sem.2004.18.5.645

Soroushian P, Obaseki K, Rojas MC (1987) Bearing strength and stiffness of concrete under reinforcing bars. ACI Mater J 84:179–184. https://doi.org/10.14359/1885

Uzumeri SM (1977) Strength and ductility of cast-in-place beam-column joints. In: Reinforced concrete structures in seismic zones (ACI SP-53). American Concrete Institute, Detroit, MI, pp 293–350

Vuran E, Serhatoğlu C, Timurağaoğlu MÖ, Smyrou E, Bal İE, Livaoğlu R (2025) Damage observations of RC buildings from 2023 Kahramanmaraş earthquake sequence and discussion on the seismic code regulations. Bull Earthq Eng 23:1153–1182. https://doi.org/10.1007/s10518-023-01843-3

Wei G, Foroughi H, Torabian S, Eatherton MR, Schafer BW (2023) Seismic design of diaphragms for steel buildings considering diaphragm inelasticity. J Struct Eng 149:04023077. https://doi.org/10.1061/JSENDH.STENG-11832

Zapata A, Arroyo O, Bonett R (2026) Impact of modeling slabs in the earthquake response of thin reinforced concrete wall buildings. Bull Earthq Eng 24:551–580. https://doi.org/10.1007/s10518-025-02309-4

Zhang D, Fleischman RB (2016) Establishment of performance-based seismic design factors for precast concrete floor diaphragms. Earthq Eng Struct Dyn 45:675–698. https://doi.org/10.1002/eqe.2679

Zhang D, Fleischman RB, Schoettler MJ, Restrepo JI, Mielke M (2019) Precast diaphragm response in half-scale shake table test. J Struct Eng 145:04019024. https://doi.org/10.1061/(ASCE)ST.1943-541X.0002304

9 ACKNOWLEDGEMENTS

The authors acknowledge the Texas Advanced Computing Center (TACC) at The University of Texas at Austin for providing high-performance computing resources that have contributed to the research results reported within this paper. The authors thank the BNCS research team for documenting and archiving the test program.

10 FUNDING

This material is based upon work supported by the National Science Foundation under Award No. (NSF 2242605). Any opinions, findings and conclusions or recommendations expressed in this material are those of the authors and do not necessarily reflect the views of the National Science Foundation.

11 AUTHOR CONTRIBUTIONS

Pratik Patra: Conceptualization, Methodology, Software, Validation, Formal analysis, Investigation, Data curation, Visualization, Writing – original draft. Travis E. Thonstad: Conceptualization, Methodology, Visualization,

Funding acquisition, Writing – review & editing. Dawn E. Lehman: Conceptualization, Methodology, Funding acquisition, Writing – review & editing.

12 DATA AVAILABILITY

The datasets generated and/or analyzed during the current study are available from the corresponding author on reasonable request.

13 DECLARATIONS

Competing interests: The authors declare that they have no known competing financial interests or personal relationships that could have appeared to influence the work reported in this paper.